STAG proteins promote cohesin ring loading at R-loops.

Hayley Porter[1+], Yang Li[1+], Wazeer Varsally[1], Maria Victoria Neguembor[2], Manuel Beltran[3], Dubravka Pezic[1], Laura Martin[2], Manuel Tavares Cornejo[3], Amandeep Bhamra[4], Silvia Surinova[4], Richard G. Jenner[3], Maria Pia Cosma[2,5,6], Suzana Hadjur[1*]

1 Research Department of Cancer Biology, Cancer Institute, University College London, 72 Huntley Street, London, United Kingdom

2 Centre for Genomic Regulation (CRG), The Barcelona Institute of Science and Technology, 08003 Barcelona, Spain.

3 Regulatory Genomics Group, Cancer Institute, University College London, London WC1E 6BT, United Kingdom

4 Proteomics Research Translational Technology Platform, Cancer Institute, University College London, 72 Huntley Street, London, United Kingdom

5 Universitat Pompeu Fabra (UPF), Dr Aiguader 88, 08003 Barcelona, Spain

6 Institució Catalana de Recerca i Estudis Avançats (ICREA), Pg. Lluís Companys 23, 08010 Barcelona, Spain.

+ These authors contributed equally

* Correspondence: s.hadjur@ucl.ac.uk

ABSTRACT

Most studies of cohesin function consider the Stromalin Antigen (STAG/SA) proteins as core complex members given their ubiquitous interaction with the cohesin ring. Here, we provide functional data to support the notion that the SA subunit is not a mere passenger in this structure, but instead plays a key role in cohesins localization to diverse biological processes and promotes loading of the complex at these sites. We show that in cells acutely depleted for RAD21, SA proteins remain bound to chromatin and interact with CTCF, as well as a wide range of RNA binding proteins involved in multiple RNA processing mechanisms. Accordingly, SA proteins interact with RNA and are localised to endogenous R-loops where they act to suppress R-loop formation. Our results place SA proteins on chromatin upstream of the cohesin complex and reveal a role for SA in cohesin loading at R-loops which is independent of NIPBL, the canonical cohesin loader. We propose that SA takes advantage of this structural R-loop platform to link cohesin loading and chromatin structure with diverse genome functions. Since SA proteins are pan-cancer targets, and R-loops play an increasingly prevalent role in cancer biology, our results have important implications for the mechanistic understanding of SA proteins in cancer and disease.

KEY WORDS
Cohesin, STAG proteins, R-loops, genome.

INTRODUCTION

Cohesin complexes are master regulators of chromosome structure in interphase and mitosis. Accordingly, mutations of cohesin subunits leads to changes in cellular identity, both during development and aberrantly in cancer [1-3]. A prevailing model is that cohesin contributes to cell identity changes in large part by dynamically regulating genome organization and mediating communication between distal regulatory elements [4-10]. Our understanding of how cohesin's component parts contribute to its functions and where cohesin becomes associated to chromatin in order to perform its critical roles in spatial genome organization is incomplete.

Most studies of cohesin function consider the Stromalin Antigen (STAG/SA) proteins as core complex members given their ubiquitous interaction with the tripartite cohesin ring (composed of SMC1, SMC3 and SCC1/RAD21). Rarely is the SA subunit considered for its roles outside of cohesin, even though it is the subunit most commonly mutated across a wide spectrum of cancers [1,11,12]. SA proteins play a role in cohesin's association with DNA [13,14]. The yeast SA orthologue is critical for efficient association of cohesin with DNA and its ATPase activation [13,14]. Recent crystallization studies of cohesin in complex with its canonical loader NIPBL[15], suggest that NIPBL and SA together wrap around both the cohesin ring and DNA to position and entrap DNA [16-18], implying a role for SA in the initial recruitment of cohesin to DNA alongside NIPBL. Further, SA proteins bridge the interaction between cohesin and CTCF [16,19,20], and also bridge interactions with specific nucleic acid structures *in vitro*. SA1 binds to AT-rich telomeric sequences [21,22] and SA2 displays sequence-independent affinity for particular DNA structures commonly found at sites of repair, recombination, and replication [23]. Consistent with this, results in yeast implicate non-canonical DNA structures in cohesin loading in S-phase. *In vitro* experiments show that cohesin captures the second strand of DNA via a single-strand intermediate [24], and chromatid cohesion is impaired by de-stabilisation of single-strand DNA intermediates during replication [25]. Together, this implicates SA proteins in playing a regulatory role in guiding or stabilising cohesin localisations.

During transcription, the elongating nascent RNA can hybridise to the template strand of the upstream DNA and form an R-loop, which is an intermediate RNA:DNA hybrid conformation with a displaced single strand of DNA (Richardson, 1975; Roy

57 and Lieber, 2009; El Hage *et al.*, 2010; Roy *et al.*, 2010). A multitude of processes
58 have been linked to R-loop stability and metabolism. For example, proper co-
59 transcriptional RNA processing, splicing, and messenger ribonucleoprotein (mRNP)
60 assembly counteract R-loop formation (Li and Manley, 2005; Teloni *et al.*, 2019). R-
61 loop structures have also been shown to regulate transcription of both mRNA and
62 rRNAs by recruitment of transcription factors, displacement of nucleosomes, and
63 preservation of open chromatin (Dunn and Griffith, 1980; Powell *et al.*, 2013; Boque-
64 Sastre *et al.*, 2015). Hence, like at the replication fork, sites of active transcription
65 accumulate non-canonical nucleic acid structures.

66 We set out to investigate the nature of the association between SA proteins and
67 CTCF. We discovered that far from being 'passengers' in the cohesin complex, SA
68 proteins perform critical roles in their own right, directing cohesin's localization and
69 loading to chromatin. In cells acutely depleted of RAD21, SA proteins remain
70 associated with chromatin and CTCF where they are enriched at 3D clustered sites of
71 active chromatin. Moreover, we identify cohesin-independent binding of SA1 to
72 numerous proteins involved in RNA processing, ribosome biogenesis, and translation.
73 Consistent with this, SA1 and SA2 interact with RNA and non-canonical nucleic acid
74 structures in the form of R-loops where SA1 acts to suppress R-loop formation.
75 Importantly, SA proteins are required for loading of cohesin to chromatin in cells
76 deficient for NIPBL, and loading is enhanced by modulating the levels of R-loop
77 structures. Our results highlight a central role for SA proteins in cohesin biology.
78 Through their diverse interactions with proteins, RNA and DNA, SA proteins act as the
79 'seed' for cohesin loading to chromatin. Finally, the interaction of cohesin-independent
80 SA proteins with nucleolar and RNA processing factors, opens up a new
81 understanding of how cohesin mis-regulation can impact disease development that
82 moves us beyond its control of gene expression regulation.

83 **RESULTS**

84

85 **SA interacts with CTCF on chromatin in the absence of the cohesin trimer.**

86 To determine how CTCF and cohesin assemble on chromatin, we used human
87 HCT116 cells engineered to carry a miniAID tag (mAID) fused to monomeric Clover
88 (mClover) at the endogenous Rad21 locus and *OsTIR1* under the control of CMV
89 (herein RAD21^{mAC}) [26]. RAD21^{mAC} cells were cultured in control conditions (ethanol) or
90 in the presence of auxin (IAA) to induce rapid RAD21 degradation. We used
91 immunofluorescence (IF) to monitor the levels of mClover, SA1, SA2 and CTCF
92 (Fig.1a, b, S1a). While acute IAA treatment robustly reduced mClover levels by over
93 83% compared to control cells, SA2 levels were reduced by 63% (p=4.7E-76), and
94 SA1 was only reduced by 29% (p=7.9E-12) (Fig.1b). We also observed a variable
95 effect on CTCF in the absence of RAD21 (reduced mean value between 7-24%). The
96 retention of SA proteins on chromatin despite the degradation of RAD21 was
97 surprising given the fact that they are considered to be part of a stable biochemical
98 complex.

99 We sought to validate these observations using an orthogonal technique and
100 to establish whether the residual SA proteins retained the capacity to directly interact
101 with CTCF. We prepared chromatin extracts from RAD21^{mAC} cells treated with ethanol
102 or IAA and established a chromatin co-immunoprecipitation (coIP) protocol to probe
103 the interactions between SA proteins, cohesin core subunits and CTCF. Both SA1
104 and SA2 interacted with RAD21 and CTCF in control cells as expected [27,28], with
105 notable differences in their preferred interactions (Fig.1c). SA2 more strongly enriched
106 RAD21 while the SA1-CTCF interaction was significantly stronger than SA2-CTCF
107 (Fig.1c). Upon RAD21 degradation, we again observed a stronger effect on chromatin-
108 bound SA2 levels compared to SA1, implying stable binding of SA2 to chromatin is
109 more sensitive to cohesin loss than SA1. Not only did the residual SA proteins retain
110 their ability to interact with CTCF in the absence of Rad21, but the interactions
111 between SA1 and CTCF were further enhanced (Fig.1c). Reciprocal coIPs with CTCF
112 confirmed the CTCF-SA interactions in RAD21-depleted cells (Fig.1d). These results
113 were validated in a second cell line and upon siRNA-mediated knockdown of SMC3,
114 confirming the results (Fig S1b).

115 We performed two-color Stochastic Optical Reconstruction Microscopy
116 (STORM) to further assess the nuclear distribution and colocalization of SA1, SA2 and
117 CTCF with nanometric resolution in RAD21-degraded cells. Upon IAA treatment, we
118 observed a decreased density of detected SA1, SA2 and CTCF in two analyzed clones
119 (Fig.1e, f, S1c, d), suggesting that RAD21 degradation affects the stability of CTCF in
120 addition to SA proteins. As we observed by conventional confocal microscopy, SA2
121 localizations were more affected than SA1 (mean density reduction in SA1, 32% vs
122 SA2, 42%). Accordingly, SA1, SA2 and CTCF clusters were more sparsely distributed
123 across the nucleus upon RAD21 degradation as quantified by nearest neighbor
124 distance (NND) analysis of protein clusters (Fig.1g). This analysis also revealed a
125 higher density of SA1 and CTCF clusters compared to SA2, with shorter distances
126 between clusters, even in ethanol conditions (Fig.1g). To further confirm that SA and
127 CTCF were still co-localised in IAA conditions, we analyzed the relative distribution of
128 SA clusters to CTCF clusters by analyzing the NND distribution between SA1 and
129 CTCF, and SA2 and CTCF. NND showed that the association between SA1 and SA2
130 with CTCF is maintained upon RAD21 degradation as compared to both the control
131 cells and to a simulation of randomly-distributed protein clusters at the same density
132 (Fig. 1h). Interestingly, while the probability of SA1 at CTCF is only modestly affected
133 in IAA conditions, supporting their continued co-localization, SA2 at CTCF is more
134 affected in IAA treated cells, in line with results indicating that SA2 levels are more
135 affected than SA1 when cohesin is depleted. Together, our results confirm the
136 maintained interaction and localization patterns of SA proteins with CTCF and reveal
137 a difference in SA paralogue stability in the absence of the core cohesin trimer.
138
139 **Cohesin-independent SA proteins are localised at clustered regions in 3D.**
140 Previous analyses of the contribution of SA proteins to genome organization [7,9] were
141 performed in cells containing cohesin rings, possibly obscuring a functional role for SA
142 proteins themselves in genome organization. To determine if cohesin-independent SA
143 proteins may function at unique locations in the genome, we investigated whether the
144 residual SA-CTCF complexes (herein, SA-CTCF$^{\Delta Coh)}$ in IAA-treated RAD21^{mAC} cells
145 (Fig.1c, d) occupied the same chromatin locations as in control cells. Using chromatin
146 immunopreciptation followed by sequencing (ChIP-seq), we determined the binding

147 profiles of CTCF, SA1, SA2, RAD21 and SMC3 in RAD21^{mAC} cells treated with ethanol
148 or IAA. Pairwise comparisons of CTCF ChIP-seq with RAD21 or SA in control
149 RAD21^{mAC} cells revealed the expected overlap in binding sites (Fig.1i, S1e). In
150 contrast, both global and CTCF-overlapping RAD21 and SMC3 ChIP-seq signals were
151 dramatically lost in IAA-treated cells (Fig.1i, S1e). In agreement with our microscopy
152 and biochemistry results, we detected residual SA1 and SA2 binding sites in IAA-
153 treated cells which retained a substantial overlap with CTCF (Fig.1i, S1e). We
154 confirmed that the sites co-occupied by CTCF and SA proteins in RAD21-depleted
155 cells were previously bound in control conditions, indicating that CTCF and SA
156 maintain occupancy at their canonical binding sites in the absence of RAD21. This
157 suggests that SA interaction with CTCF in the absence of the cohesin ring is a step in
158 normal cohesin activity.
159 While depletion of cohesin results in a dramatic loss of Topologically
160 Associated Domain (TAD) structure [8], the frequency of long-range inter-TAD, intra-
161 compartment contacts (LRC) is increased [5,8], and enriched for CTCF [5] or active
162 enhancers [8]. To determine whether residual, chromatin-bound SA could be associated
163 with LRCs in the absence of RAD21, we re-analysed Hi-C data from control and IAA-
164 treated RAD21^{mAC} cells [8]. We quantified all contacts within two different scales of
165 genome organization; local TAD topology (100k-1Mb) and clustered LRCs (1-5Mb)
166 (Fig.1j). As previously shown, local TAD contacts are lost and clustered LRCs are
167 enriched in IAA conditions (Fig.1j). When we probed the Hi-C datasets for contacts
168 containing the residual SA-CTCF$^{\Delta Coh}$ binding sites, we observed a further enrichment
169 in IAA conditions (Fig.1j, bottom row), indicating that SA-CTCF$^{\Delta Coh}$ are enriched at the
170 clustered LRCs formed when cells are depleted of cohesin and thus implicating them
171 in 3D structural configurations. Finally, using ChromHMM, we discovered that SA-
172 CTCF$^{\Delta Coh}$ sites are characterised by active chromatin and enhancers (Fig.S1f). Our
173 results suggest that cohesin-independent SA, either with CTCF or alone, may itself
174 contribute to large-scale arrangement of active chromatin and regulatory features in
175 3D space.
176
177
178

179 **SA interacts with diverse 'CES-binding proteins' in RAD21-depleted cells.**
180 SA proteins contain a highly conserved domain termed the 'stromalin conservative
181 domain' [14,29], or the 'conserved essential surface' (CES). Structural analysis of CTCF-
182 SA2-SCC1(RAD21) has recently shown that FGF (F/YxF) motifs in the N-terminus of
183 CTCF bind to the CES on the SA2-SCC1 sub-complex, forming a tripartite interaction
184 patch [16]. Furthermore, the authors identified an FGF-like motif in additional cohesin
185 regulators and showed that a consensus motif could be used to predict interaction with
186 additional chromatin proteins. Thus, we investigated whether SA could associate with
187 other FGF-motif containing proteins in native and IAA conditions in cells. We
188 performed chromatin IP with SA1 and SA2 in ethanol and IAA and probed for
189 interaction with CTCF, and three additional FGF-motif containing proteins, CHD6,
190 MCM3 and HNRNPUL2 (Fig.2a, S2a). As with CTCF, all of the proteins directly
191 interacted with SA1 in RAD21-control cells and furthermore their interaction with SA1
192 was enriched upon RAD21-degradation. Interestingly, despite SA2 also containing the
193 conserved 'CES' domain, the FGF-motif proteins did not interact with SA2 as strongly
194 (Fig.2a), pointing to an additional element which functions to stabilise SA with FGF-
195 containing proteins *in vivo*. These results revealed that SA can interact with proteins
196 beyond just CTCF in the absence of cohesin, indicating a need to re-evaluate the role
197 of SA in cohesin activity and consider possible novel functions for SA proteins.
198
199 **SA1 interacts with a diverse group of proteins in the absence of cohesin.**
200 To delineate novel protein binding partners and putative biological functions of SA1,
201 we optimised our chromatin-bound, endogenous SA1 co-IP protocol to be compatible
202 with mass-spectrometry (IP-MS) and used this to comprehensively characterize the
203 SA1 protein–protein interaction (PPI) network in control or RAD21-degraded
204 RAD21^{mAC} cells. Three biological replicate sets were prepared from RAD21^{mAC} cells
205 that were either untreated (UT) or treated with IAA (IAA) and processed for IP with
206 both SA1 and IgG antibodies. In parallel, RAD21^{mAC} cells were also treated with
207 scrambled siRNAs or with siRNA to SA1 to confirm the specificity of putative
208 interactors (Fig. S2b). Immunoprecipitated proteins were in-gel Trypsin digested, gel
209 extracted, and identified by liquid chromatography tandem mass spectroscopy (LC-

210 MS/MS). SA1 peptides were robustly detected in all UT and siCON samples and never
211 detected in IgG controls, validating the specificity of the antibody.

212 We identified 1282 unique proteins that co-purified with SA1 with a False
213 Discovery Rate <1%. After filtering steps (methods), we used a pairwise analysis of
214 IAA vs UT samples to generate a fold-change value for each putative interactor. These
215 candidates were found in at least 2 of the 3 SA1 IP replicates, were changed by at
216 least 1.5-fold compared to UT controls, and sensitive to siSA1, yielding 134 high-
217 confidence cohesin-independent SA1 ($SA1^{\Delta Coh}$) interactors (Fig. 2b, Table 1). As
218 expected, core cohesin subunits SMC1A and SMC3 were strongly depleted while no
219 peptides were detected for RAD21 (Fig. 2b). SA1 itself was significantly depleted
220 compared to control cells, as were other cohesin regulators, known to directly interact
221 with SA1, such as PDS5B [30]. In line with the enrichment we observed for the CES-
222 binding proteins in IAA-conditions (Fig. 1c, 2a), the vast majority of the $SA1^{\Delta Coh}$
223 interactors were enriched for binding with SA1 in IAA conditions (117 of 134) (Fig. 2b).

224 We used STRING analysis to compute the associations between our $SA1^{\Delta Coh}$
225 interactome and to identify enriched biological processes and molecular functions.
226 This revealed that the $SA1^{\Delta Coh}$ PPI network included gene expression, chromatin,
227 cytoplasmic and RNA binding proteins representing a variety of functionally diverse
228 cellular processes. Among these are processes previously associated with cohesin
229 biology and identified in published cohesin mass-spec experiments [31], thus validating
230 our approach, such as MCM3 and SWI/SNF components INO80 and SMARCAL1
231 which are involved in DNA replication and chromatin remodelling, respectively.
232 Similarly, several transcriptional and epigenetic regulators were identified, such as
233 PRC2 component JARID2 and TAF15 and SPTY2D1.

234 In addition, we identified proteins associated with SA1 in IAA conditions that
235 were involved in functions that have not been previously associated with SA biology
236 (Fig. 2c, d). The most enriched category was RNA processing ($p=3.62^{-39}$), and
237 included proteins involved in RNA modification (YTHDC1, ADAR1, FTSJ3); mRNA
238 stabilization and export (SYNCRIP, FMR1); and several RNA splicing regulators
239 (SRSF1, SON). Accordingly, we found a significant enrichment for DNA and RNA
240 helicases ($p=3.54^{-08}$) (MCM3, DHX9, more) and RNA binding proteins ($p=9.11^{-11}$)

241 within which were serveal hnRNP family members (hnRNPU or SAF-A). We also found
242 a highly significant enrichment of proteins associated with Ribosome biogenesis
243 ($p=2.20^{-30}$) including both large and small subunit components (RPL5, 17, 29, RPS9);
244 rRNA processing factors (BOP1, NOP56); and components of the snoRNA pathway.
245 Translation was significantly enriched as a biological process ($p=1.64^{-06}$), with several
246 cytoplasmic translation regulators also identified as $SA1^{\Delta Coh}$ interactors (Fig. 2c, d).
247 Among these are ESYT2 and EIF3B which we identify as FGF-containing proteins that
248 are primarily found in the cytoplasm (Fig. 2d). We validated 8 of the highest-ranking
249 proteins within the enriched functional categories described above by immunoblotting
250 in ethanol and IAA-treated $RAD21^{mAC}$ cells (Fig. 2d). Overall, our results show that
251 $SA1^{\Delta Coh}$ PPIs contain not only for transcriptional and epigenetic regulators, but also
252 are predominantly enriched for proteins with roles in nuclear RNA processing and
253 modification, ribogenesis and translation pathways. Accordingly, this suggests that SA
254 may facilitate an aspect of cohesin regulation at a variety of functionally distinct cellular
255 locations through its association with these diverse proteins.

256

257 **SA proteins directly bind RNA.**

258 Since RNA binding and RNA processing were two of the most enriched categories in
259 the $SA1^{\Delta Coh}$ PPI network, we asked whether SA proteins could also bind RNA. We
260 performed CLIP (crosslinking and immunoprecipitation) to determine whether SA
261 proteins directly bind RNA in untreated $RAD21^{mAC}$ cells. We found that both SA1 and
262 SA2 directly bound RNA (Fig.3a). This was evidenced by detection of RNPs of the
263 expected molecular weights, with a smear of trimmed RNA, which was stronger in the
264 +UV and +PNK conditions, which increased as the RNaseI concentration was reduced
265 and which was lost after siRNA-mediated KD (Fig.3a, S3a). We repeated the
266 experiment in IAA-treated $RAD21^{mAC}$ cells to determine if the SA subunits can directly
267 bind RNA in the absence of cohesin. Although RAD21 depletion reduced SA1 and
268 SA2 stability, the amount of RNA crosslinked to the proteins remained proportional to
269 the amount of SA1 and SA2 protein, demonstrating that cohesin is not required for the
270 interaction of these proteins with RNA in cells (Fig.3b, S3b. Thus, cohesin-
271 independent SA proteins interact with a wide array of RNA binding proteins (RBP) as
272 well as with RNA itself.

273 **A variable exon in the C-terminus of SA tunes association w RNA binding**
274 **proteins.**
275 SA1 and SA2 express transcript variants in RAD21^{mAC} cells. One such prominent
276 variant arises from the alternative splicing of a single C-terminal exon, exon 31 in SA1
277 (SA1$^{e31\Delta}$) and exon 32 in SA2 (SA2$^{e32\Delta}$) (Fig.3c). This has been observed in many cell
278 types, however the significance of this variant is unknown. We re-analysed publicly
279 available RNA-seq datasets for gene expression and alternative splicing. Interestingly,
280 quantification of the splicing profiles using VAST-tools analysis [32] revealed that the
281 frequency of the e31 or e32 splicing events were dramatically different (Fig.3d). The
282 majority of SA1 mRNAs *include* e31 (average PSI 97.7%), while the majority of SA2
283 mRNAs *exclude* e32 (average PSI 20.4%). We confirmed this at the protein level by
284 designing custom esiRNAs to specifically target SA1 e31 or SA2 e32 (Methods).
285 Smartpool (SP) KD reduced the levels of SA1 and SA2 to similar extents compared to
286 scrambled controls (87% and 94% respectively compared to siRNA control) (Fig. 3e,
287 f). Specific targeting of SA1 e31 led to a reduction of 85% of SA1 compared to esiRNA
288 control (Fig.3e), while SA2 e32 targeting had a minimal effect on SA2 protein levels
289 compared to its esiRNA control (reduction of 2%) (Fig.3f), in line with the PSI data.
290 These results imply that cells 'tune' the availability of e31/32 domains in SA
291 proteins, prompting us to investigate the nature of these exons to shed light on their
292 potential function. Inspection of the amino acid (aa) sequence of the spliced exons
293 revealed that they encode a highly basic domain within an otherwise acidic C-terminus
294 (Fig.3c). Overall, the SA paralogs are highly homologous, however the N and C termini
295 diverge in their aa sequence. Despite this divergence, e31 and e32 have retained their
296 basic properties with a pI similar to histones (pI=10.4, 9.9 for e31 and e32,
297 respectively) (Fig.3c). Basic domains act as important regulatory cassettes and can
298 bind nucleic acids. Thus, we investigated whether the alternatively spliced basic exon
299 of SA proteins contributes to the differential association of SA with RNA (Fig.3a,b).
300 We cloned cDNAs from HCT116 cells representing full-length SA2 (SA2^{FL}) and the
301 variant lacking e32 (SA2$^{e32\Delta}$), tagged them with YFP and expressed them in HCT cells
302 (Fig.S3c). We used the GFP-TRAP system to specifically purify the YFP-tagged
303 isoforms from cells and compared their ability to interact with RNA. While CLIP
304 experiments revealed that the presence of the alternative e32 does not affect the
305 ability of SA2 to interact with RNA (Fig.3g, S3d), however it did reveal bands which

306 were enriched in the YFP-SA2^{FL} CLIP and not observed in the YFP-SA2$^{e32\Delta}$ samples,
307 revealing a role for the alternative exon in enhanced association of SA2 with RNA
308 binding proteins.
309
310 **SA proteins bind to endogenous R-loops.**
311 Regulators of RNA processing, such as splicing, modification and export factors, act
312 as regulators of R-loops [33]. In addition, R-loops are found at sites of multiple biological
313 processes including transcription (of both mRNAs and rRNA), DNA replication and
314 DNA repair [33]. Given the fact that many of these processes were enriched in the SA1
315 interactome and our observations that SA proteins can interact with RNA, we reasoned
316 that the diversity of biological processes represented in the SA1$^{\Delta Coh}$ PPI network may
317 be reflective of a role for SA proteins in R-loop biology.
318 To address this, we returned to our IP-MS experiment to analyse enrichment of
319 R-loop-associated proteins in our SA1$^{\Delta Coh}$ interactome. We overlapped the proteins
320 identified in two independent IP-MS experiments using the R-loop specific antibody,
321 S9.6 [34,35] to create a custom high-confidence 'R-loop interactome' and then used a
322 hygrometric distribution to determine the significance of this category in the SA1$^{\Delta Coh}$
323 interactome (methods). Both the custom R-loop interactome as well as the S9.6
324 interactomes from Cristini et al., and Wang et al., were highly over-enriched in the
325 SA1$^{\Delta Coh}$ interactome (FDR=1.10x10^{-15}, 1.38x10^{-47}, respectively) (Fig.4a). As an
326 independent validation of these observations, we optimised an S9.6 coIP method in
327 RAD21^{mAC} cells (Fig.4b, methods). In agreement with published results, we found that
328 S9.6 precipitated with the known R-loop helicases AQR, DHX9, RNase H2 [34,36] as well
329 as MCM3 and RNA Pol II [37]. Both SA1 and SA2 precipitated with S9.6 (Fig.4b, S3x),
330 indicating a function at R-loops and supporting the observed enrichment of R-loop
331 proteins in the SA1 interactome.
332 To understand the causal relationship between R-loops and SA proteins, and
333 to determine the specificity of S9.6-SA interactions, we used RNase H1 to selectively
334 degrade the RNA component of RNA:DNA hybrids [38]. We were able to achieve a
335 ~30% reduction in R-loops upon treatment of chromatin lysates with RNase H (Fig.4b,
336 S4a). This reduction was proportional to the observed reduction in coIP of SA1 by
337 S9.6 (Fig.4b, S4b). In parallel, we assessed the effect of R-loop degradation on

338 chromatin-bound SA levels in single cells using confocal microscopy. Treatment of
339 RAD21^{mAC} cells with RNase H1 reduces S9.6 staining by >50% of untreated controls
340 (Fig.4c, d). In agreement with the S9.6 coIP results, mean levels of SA1 and SA2 were
341 significantly reduced by 35% and 18.5%, respectively compared to control cells in
342 response to RNase H treatment (Fig. 4c, d). Finally, we also depleted R-loops *in vivo*
343 by overexpressing ppyCAG-v5-RNaseH1 in cells. IF revealed that nuclear S9.6 levels
344 were significantly reduced in cells which expressed v5 (to 38% of controls) and that
345 mean levels of chromatin-associated SA1 were similarly reduced by 29.4% (p=4.05E-
346 8) (Fig.S4c), further confirming the causal relationship between R-loops and SA
347 proteins.

348

349 **SA1 proteins act as suppressors of R-loops.**

350 Proteins that act to suppress R-loops *in vivo*, such as AQR [36], have an inverse
351 correlation with S9.6 levels. From our IF results (Fig. 4c, d), we noticed that SA1 had
352 a similar negative relationship with S9.6 (Fig. S4d), prompting us to investigate
353 whether SA proteins could act as suppressors of R-loop formation. To this end, we
354 treated RAD21^{mAC} cells with scramble control siRNAs or siRNA to SA1, SA2 or AQR
355 and used IF to assess the impact on nuclear S9.6 levels in KD cells (Fig.4e, f). As
356 previously reported, AQR KD resulted in a 30.1% increase of mean nuclear S9.6 levels
357 (p=0.0004). Compared to control siRNA-treated cells, mean SA1 levels were reduced
358 by 56.2% (p=4.1E-40), while mean nuclear S9.6 staining was significantly increased
359 in the same cells by 55.3% (p=3.90E-08) (Fig.3f, g). We note that perturbing SA1
360 levels increased nuclear S9.6 staining to a similar extent as what was observed upon
361 AQR KD, a bonafide R-loop regulator. When we treated cells with the custom siRNA
362 to SA1 e31 (Fig 3e), we also observed an increase in S9.6 signals (Fig S4e),
363 suggesting that this basic exon plays a role in R-loop stability. Surprisingly, despite
364 efficient KD of SA2 (68% reduction), there was no significant change in nuclear S9.6
365 staining (mean S9.6 reduced by 10% compared to control, p=0.17), indicating that
366 although SA2 is localised to R-loops (Fig S4b), it does not seem to contribute to their
367 regulation. Taken together, our results confirm the presence of SA proteins at
368 endogenous R-loops *in vivo* and reveal a role for SA1 in R-loop suppresion.

369

370 **SA contributes to cohesin loading independently of NIPBL.**

371 Our results thus far support a hypothesis whereby $SA^{\Delta Coh}$ engages with RNA and
372 various RNA binding proteins at clustered regulatory regions (possibly R-loops) to
373 structurally support them and/or facilitate cohesin's association with chromatin.
374 Indeed, several lines of evidence suggest that alongside the canonical NIPBL/Mau2
375 loading complex, SA proteins contribute to cohesin's association with chromatin. In
376 yeast, interaction of the SA orthologue with the loader complex is required for efficient
377 association of the cohesin ring with DNA and subsequent ATPase activation [13,14].
378 Separating interactions into SA-loader and cohesin ring-loader subcomplexes still
379 impairs cohesin loading, indicating that SA functions as more than just a bridge protein
380 [14]. Crystallisation studies reveal a striking similarity of NIPBL and SA, in that both are
381 highly bent, HEAT-repeat proteins [39,40]. Indeed, NIPBL and SA1 interact together in
382 an antiparallel arrangement and wrap around DNA and the cohesin ring via similar
383 interactions in their respective 'U' surfaces, implying that SA1 has a role in the initial
384 recruitment of cohesin to DNA alongside NIPBL (Shi 2020, Higashi 2020).

385 The $RAD21^{mAC}$ system has the unique advantage that when IAA is washed off
386 cells, RAD21 proteins are no longer degraded and can be 're-loaded' back onto
387 chromatin (Fig.5a). We coupled this to an siRNA-mediated KD of NIPBL to investigate
388 whether cohesin re-loading onto chromatin is influenced by SA proteins in human cells
389 in native conditions. $RAD21^{mAC}$ cells were treated with scramble or NIPBL siRNAs and
390 subsequently grown in ethanol or IAA. The '0h post IAA wash-off' sample represents
391 the extent of cohesin *degradation* in the IAA-treated cells. In parallel, IAA was washed
392 out and the cells were left for 4h to recover. This sample, '4h post IAA wash-off'
393 represents the extent of cohesin *re-loading* in the respective genetic background
394 (Fig.5a, b). We confirmed loss of the loader complex by immunoblot for both NIPBL
395 and MAU2 as it is known that MAU2 is de-stablised upon NIPBL loss [41]. We note that
396 re-loading was not fully restored to the levels observed in ethanol-treated cells and
397 varied between experiments (Fig.5c), which may reflect differences in the initial
398 amounts of RAD21 or NIPBL (see methods). Despite this variation, we observed a
399 consistent effect on RAD21 re-loading across 8 independent experiments. As
400 expected, in NIPBL KD conditions, mean RAD21 re-loading efficiency was reduced to
401 40.9% of the siRNA controls (mean re-loading siNIPBL, 2.1 vs siCon, 3.6), however

402 this did not represent a statistically significant difference (p=0.33) and accordingly, a
403 large fraction of chromatin-associated RAD21 could still be detected in NIPBL KD cells
404 (Fig. 5c), indicating that cells have a NIPBL-independent cohesin re-loading
405 mechanism.

406 We performed the same experiment and this time, in addition to treating cells
407 with siRNAs to NIPBL, we also included siRNA to SA1 and SA2 together (siSA), and
408 a siNIPBL+ siSA condition to ask if SA proteins contribute to the observed NIPBL-
409 independent reloading. Across 5 independent experiments, SA KD had a more
410 dramatic effect on cohesin re-loading efficiency than NIPBL KD, reducing RAD21 re-
411 loading on chromatin to 51% of scramble controls (mean re-loading siSA, 1.9 vs siCon,
412 5.1, p=0.061), (Fig. 5d, e). However, only when SA and NIPBL were both reduced in
413 cells, was there a statistically significant change to cohesin re-loading, reducing
414 RAD21 on chromatin to 64.9% of scramble control cells (mean re-loading
415 siNIPBL+siSA, 1.42 vs siCon, 5.1, p=0.001), indicating that SA performs an important
416 and complementary step to NIPBL and MAU2 during normal reloading (Fig.5d, e).

417 Finally, given that SA localises to R-loops and these can be localized to many
418 places across the genome, we reasoned that SA could use this structural platform to
419 link the loading of cohesin to diverse biological processes. Therefore, we repeated the
420 cohesin re-loading experiments in the presence of siRNAs to AQR, which we had
421 previously shown act as suppressors of R-loops (Fig. 4e, f). AQR KD alone had little
422 effect on cohesin re-loading efficiency (Fig. 5f, g), however when R-loops were
423 increased in the context of reduced NIPBL, we observed an increase in the efficiency
424 of cohesin re-loading compared to control cells (Fig. 5f, g). This increase in re-loading
425 efficiency corresponded with a 2.08-fold increase in SA1 levels and a 1.46-fold
426 increase in s9.6 levels, relative to siCon (Fig. S5a) while MAU2 and AQR showed a
427 corresponding fold-change of 0.48 and 0.69, respectively, indicating the specificity of
428 SA1 and R-loop increase. Our results support a role for R-loops in SA-mediated
429 cohesin loading.
430

431 **DISCUSSION**

432 Whether SA proteins function in their own right outside of the cohesin complex is rarely
433 considered. Consequently, our understanding of how these proteins contribute to
434 cohesin function and disease is incomplete. In this study, we shed light on this
435 question by uncovering a diverse repertoire of SA interactors in cells acutely depleted
436 for the cohesin trimer. These range from proteins associated with translation and
437 ribogenesis to RNA processing factors and regulators of the epitranscriptome. These
438 observations suggest that SA proteins have a previously unappreciated role in post-
439 transcriptional regulation of gene expression which offers much-needed new insight
440 into its roles in disease and cancer.

441 Acute depletion of the cohesin ring has allowed us to capture a moment in the
442 normal life cycle of cohesin – DNA associations and unveiled a previously
443 unappreciated step for SA proteins. We show that cohesin-independent SA proteins
444 bind to DNA and RNA, in the context of non-canonical RNA:DNA hybrid structures as
445 we have shown here, or sequentially, and use this platform for the loading of cohesin
446 to chromatin. Our results are supportive of biophysical observations of SA proteins
447 and R-loops [42] and *in vitro* assessment of cohesin loading at DNA intermediates [24].
448 Structural studies suggest that NIPBL and SA1 together bend DNA and cohesin to
449 guide DNA entering into the cohesin ring [17,18,43]. Our work shows that in cells lacking
450 either the canonical NIPBL/MAU2 loader complex or the SA proteins, cohesin can still
451 associate with chromatin, suggesting that loading can occur with either component
452 alone, albeit most effectively together.

453 Since SA paralogues have distinct terminal ends and nucleic acid targeting
454 mechanisms [22,23], their initial recruitment to chromatin may be specified by unique
455 DNA, RNA or protein-interactions, or indeed all three. Such diversification of loading
456 platforms would be important in large mammalian genomes to ensure sufficient
457 cohesin was chromatin associated or to direct stabilization of particular biological
458 processes for a given cell fate [44]. Indeed, SA1 and SA2 show clear differences in
459 interaction with FGF-motif containing proteins, despite the fact that both paralogs
460 contain a CES domain [45], underscoring the importance of *in vivo* studies and arguing
461 that additional factors play an important role in complex stabilization. In this context,
462 RNA-associated protein interaction has previously been shown to support cohesin

463 stabilisation at CTCF at the *IGF2/H19* locus [46]. These results are in line with our
464 findings that a basic domain in the unstructured C-terminal portion of SA supports
465 RNA-associated protein interactions and R-loop stability.

466 This study identifies SA proteins as novel regulators of RNA:DNA hybrid
467 homeostasis. It is noteworthy that other suppressors of R-loop formation include
468 mRNA processing factors, chromatin remodellers and DNA repair proteins [47] which all
469 function in the context of nuclear bodies [48]. We find that SA proteins are enriched at
470 very distal chromatin interactions in cohesin-depleted Hi-C data and they interact with
471 numerous RNA binding proteins known to condense in 3D [49,50]. Harnessing such
472 condensates would provide an efficient loading platform for cohesin at sites of similar
473 biological function. If SA paralogs direct different localization of cohesin loading or
474 stability of its association, this could have important implications in our understanding
475 of disease and cancer.

ACKNOWLEDGMENTS

This work would not be possible without the support of a Senior Research Fellowship from the Wellcome Trust awarded to S.H. (106985/Z/15/Z) and a CRUK PhD studentship awarded to H.P. The Proteomics work was supported by the CRUK–UCL Centre Award [C416/A25145]. We thank Stanimir Dulev for his contributions at the early stages of the project. We would like to thank Konstantina Skourti-Stathaki for advice about S9.6 IFs and R-loops. We are grateful to the members of the Hadjur lab for critical discussions and reading of the manuscript.

AUTHOR CONTRIBUTIONS

H.P. and S.H. conceived the project. H.P. designed and performed all the coIP, Mass spectrometry and cohesin re-loading experiments, analysed the ChIP and Hi-C data and performed the statistical analysis for mass spectrometry with the support of A.B. and S.S. Y.L. performed and analysed all imaging experiments (apart from STORM), derived clonal lines of RAD21-mAC cells, cloned YFP-tagged SA2 cDNAs and performed CLIP together with M.T.C. W.V. performed Hi-C, ChIP-seq and splicing analyses. M.V.N., L.M. and M.P.C. performed and analysed STORM imaging. D.P. discovered splicing features of the SA isoforms. H.P. and Y.L. prepared cellular materials for CLIP, which was carried out by M.B., M.T.C., and R.J. A.B. and S.S. performed mass spectrometric and proteomic analysis. H.P., Y.L and S.H. formatted all figures and wrote the manuscript with input from all authors.

Declaration of Interests

The authors declare no competing interests.

500 **FIGURE LEGENDS**
501
502 **Figure 1. SA interacts with CTCF in the absence of cohesin.**
503 A) Representative confocal images of SA1 and CTCF IF in RAD21^{mAC} cells treated
504 with ethanol (EtOH) as a control or Auxin (IAA) for 4hrs. Nuclei were counterstained
505 with DAPI.
506
507 B) Imaris quantification of the fluorescence intensity of mClover, SA1 (top panel), SA2
508 (bottom panel) and CTCF in EtOH and IAA-treated RAD21^{mAC} cells. Whiskers and
509 boxes indicate all and 50% of values respectively. Central line represents the median.
510 Asterisks indicate a statistically significant difference as assessed using two-tailed t-
511 test. * $p<0.05$, ** $p<0.005$, *** $p<0.0005$, n.s., not significant. n>50 cells/condition from
512 3 biological replicates.
513
514 Chromatin coIP of (C) SA1, SA2 and IgG with RAD21 and CTCF or (D) CTCF and
515 IgG with RAD21, SA1 and SA2 in RAD21^{mAC} cells treated with EtOH or IAA for
516 4hrs. Input represents (C) 2.5% and (D) 1.25% of the material used for
517 immunoprecipitation.
518
519 E) Dual-color STORM images of SA1 (green) and CTCF (magenta) in EtOH and IAA-
520 treated RAD21^{mAC} cells. Representative full nuclei and zoomed nuclear areas are
521 shown. Line denotes 2 microns and 200nm for full nuclei and zoomed areas
522 respectively. See supplementary Figures for SA2 STORM images.
523
524 F) Mean CTCF, SA1 and SA2 localization densities (localizations normalized with
525 nuclear area) in EtOH and IAA-treated RAD21^{mAC} cells (n = >30, >17 and >15 nuclei
526 for CTCF, SA1 and SA2 respectively). Mean and SD are plotted, Mann Whitney test.
527 **** $p<0.0001$.
528
529 G) Mean Nearest Neighbor Distance (NND) of CTCF, SA1 and SA2 clusters in
530 nanometers in EtOH and IAA-treated cells (n = >38, >14 and >23 nuclei for CTCF,
531 SA1 and SA2 respectively). Mean and SD are plotted, Mann Whitney test. ****
532 $p<0.0001$.
533
534 H) Nearest Neighbor Distance (NND) distribution plot of the distance between CTCF
535 and SA1 (left panel) or SA2 (right panel) clusters in EtOH and IAA-treated cells.
536 Experimental data are shown as continuous lines, random simulated data are
537 displayed as dotted lines.
538
539 I) ChIP–seq heat map of CTCF, SA1, SA2, Rad21 and
540 SMC3 binding profiles in control (EtOH) and IAA-treated RAD21^{mAC} cells. Selected
541 regions are bound by CTCF in control conditions.
542
543 J) Analysis of contact frequency hotspots from Hi-C libraries generated from EtOH-
544 treated (top row) and IAA-treated (bottom row) RAD21^{mAC} cells. Contact frequencies
545 were calculated in two distance ranges of 100kb – 1Mb and 1-5Mb. The last column
546 includes contact frequencies specifically at residual SA-CTCF binding sites.
547

548 **Figure 2. Characterization of SA1 protein-protein interaction network in RAD21-**
549 **depleted cells.**
550 A) Chromatin coIP of SA1, SA2 and IgG with 4 predicted CES-binding proteins in
551 RAD21^{mAC} cells treated with EtOH or IAA for 4hrs. Input represents 1.25% of the
552 material used for immunoprecipitation.
553
554 B) Volcano plot displaying the statistical significance (-log10 p-value) versus
555 magnitude of change (log2 fold change) from SA1 IP-MS data produced
556 from RAD21^{mAC} cells treated with ethanol or IAA (n=3). Vertical dashed lines represent
557 changes of 1.5-fold. Horizontal dashed line represents a pvalue of 0.1.
558 Cohesin complex members and validated high-confidence proteins have been
559 highlighted.
560
561 C) SA1$^{\Delta Coh}$ interaction network of protein–protein interactions identified in
562 RAD21^{mAC} cells using STRING. Node colours describe the major
563 enriched categories, with squares denoting helicases and polygons
564 denoting hnRNP family members. Proteins within each enrichment category were
565 subset based on p-value change in B). See supplemental figures for full network.
566
567 D) Chromatin IP of SA1 and IgG in RAD21^{mAC} cells treated with EtOH or IAA and
568 immunoblotted with antibodies to validate the proteins identified by IP-MS. Input
569 represents 1.25% of the material used for immunoprecipitation. * We note that ESYT2
570 is a FGF-containing protein.
571
572
573
574 **Figure 3. SA proteins bind to RNA.**
575 A) CLIP for SA1, SA2 and non-specific IgG controls. Autoradiograms of crosslinked
576 ^{32}P-labelled RNA are shown at the top and the corresponding immunoblots, below.
577 CLIP was performed with and without UV crosslinking and polynucleotide kinase
578 (PNK) and with high (H; 1/50 dilution) or low (L; 1/500 dilution) concentrations of
579 RNase I.
580
581 B) CLIP for SA1, SA2 and non-specific IgG control in ethanol (-) or IAA-treated
582 Rad21^{mAC} cells. ^{32}P-labelled RNA and the corresponding immunoblots are shown as
583 above.
584
585 C) Schematic of the SA1 and SA2 proteins showing the SA1-specific AT-hook, the
586 conserved CES domain (blue) and the acidic C-terminus (green) which contains
587 the basic alternatively spliced exon (red). Right-hand zoom-in indicates the spliced
588 exons for SA1 (top) and SA2 (bottom) and the pI for each. The conservation scores for
589 the divergent N- and C-termini and the middle portion of the proteins which contains
590 the CES domain are shown.
591
592 (D) Percent Spliced In (PSI) calculations for SA1 exon 31 (black) and SA2 exon 32
593 (grey) based on VAST-Tools analysis of RNA-seq from multiple datasets (see
594 Methods).
595

596 (E) Western blot analysis of SA1 levels in whole cell lysates after treatment
597 with scrambled siRNAs (siCon), SmartPool SA1 siRNAs (siSA1 SP),
598 control esiRNAs (esiCon) and esiRNA designed to target SA1 exon
599 31 for 48hrs in RAD21^{mAC} cells. H3 serves as a loading control. The percentage of
600 knockdown (KD) after SA1 signal is normalised to H3 is shown.
601
602 (F) Western blot analysis of SA2 levels in whole cell lysates after treatment with
603 scrambled siRNAs (siCon), SmartPool SA2 siRNAs (siSA2 SP),
604 control esiRNAs (esiCon) and siRNA designed to target SA2 exon 32
605 for 48hrs in RAD21^{mAC} cells. H3 serves as a loading control. . The percentage of
606 knockdown (KD) after SA2 signal is normalised to H3 is shown.
607
608 (G) CLIP with endogenous SA2 (as in A, B above), IgG control and cells where
609 either YFP-tagged full-length SA2 or YFP-tagged SA2 lacking exon 32 are expressed
610 for 48hrs. CLIP reveals proteins which specifically associate with exon-32 containing
611 SA2 (arrow).
612
613
614 **Figure 4. SA proteins act as suppressors of endogenous R-loops.**
615 (A) Adjusted p-value (FDR) for enrichment of S9.6 interactome data from Cristini et al.
616 and Wang et al., with the SA1$^{\Delta Coh}$ interactome. Overlap indicates the proteins
617 identified in both S9.6 interactome datasets, representing a high confidence R-loop
618 interactome list.
619
620 (B) Chromatin coIP of S9.6 and IgG in RAD21^{mAC} cells treated with RNase H enzyme
621 and immunoblotted with antibodies representing known R-loop proteins, as well as
622 SA1. Input represents 1.25% of the material used for
623 immunoprecipitation. Bottom, S9.6 dot blot of lysates used in coIP.
624
625 (C) Representative confocal images of S9.6, SA1 and SA2 IF in RAD21^{mAC} cells
626 treated with control buffer or RNase H enzyme. Nuclear outlines (white) are derived
627 from DAPI counterstain.
628
629 (D) Fluorescence Intensity of S9.6, SA1 and SA2 protein assessed by
630 Immunofluorescence in (C). Data are from three biological replicates with >50 cells
631 counted/condition). Quantifications and statistical analysis were done as above.
632
633 (E) Representative confocal images of S9.6 and SA1, SA2 or AQR IF in
634 RAD21^{mAC} cells treated with scramble control siRNA (si scr) or siRNA to the protein of
635 interest. Nuclear outlines (white) are derived from DAPI counterstain.
636
637 (F) Fluorescence Intensity of S9.6, SA1, SA2 and AQR proteins assessed by
638 Immunofluorescence in (E). Data are from three biological replicates with >50 cells
639 counted/condition). Quantifications and statistical analysis were done as previously
640 stated.
641
642
643

644 **Figure 5. SA proteins contribute to cohesin loading at R-loops.**
645 (A) Schematic of experimental set-up. RAD21^{mAC} cells expressing mClover (green
646 cells in dishes) were treated with scramble siRNAs or siRNA to NIPBL. Prior to
647 collection, cells were cultured in ethanol or IAA for 4hrs to degrade RAD21 (0 h
648 timepoints). Each sample was then split into those cultured in ethanol or IAA for 4hrs to
649 degrade RAD21 (0h timepoints). The IAA treatment was washed-off and the cells were
650 left to recover for 4hrs (4h timepoints). Chromatin fractions were prepared from all
651 samples and used in immunoblot analysis.
652
653 (B) Representative western blot analysis of chromatin-bound RAD21, MAU2 and
654 NIPBL levels in RAD21^{mAC} cells treated according to the schematic shown in (A). H3
655 was used as a loading control. *NB* The full blots can be seen in the supplement.
656
657 (C) RAD21 fold change relative to siCon samples at the 0h timepoint in siCon 4h (light
658 grey), siNIPBL 0hr (light blue) and siNIPBL 4hr (dark blue). Whiskers and boxes
659 indicate all and 50% of values respectively. Central line represents the
660 median. statistical analysis as assessed using a two-tailed t-test. Data is
661 from 8 biological replicates.
662
663 (D) Representative western blot analysis of chromatin-bound RAD21, SA1, SA2,
664 MAU2 and NIPBL levels in RAD21mAC cells treated according to the schematic
665 shown in (A) and including samples treated with siRNA to SA1 and SA2 together
666 (siSA) and siRNA to NIPBL + siSA. H3 was used as a loading control.
667
668 (E) RAD21 fold change relative to siCon samples at the 0h timepoint
669 in siCon, siNIPBL, siSA and siNIPBL+siSA. Asterisks indicate a statistically significant
670 difference as assessed using 2-tailed T-test. ** $p<0.005$. Data is from 5 biological
671 replicates.
672
673 (F) Representative western blot analysis of chromatin-bound RAD21, AQR, MAU2 and
674 NIPBL levels in RAD21mAC cells treated according to the schematic shown in (A) and
675 including samples treated with siRNA to AQR and siRNA to NIPBL + AQR. H3 was
676 used as a loading control. RAD21* denotes increased exposure. NIPBL levels could
677 not be determined due to incompatibility with assessing RNA:DNA hybrids. *NB* siCon
678 samples were cropped here and the full blots can be seen in the supplement.
679
680 (G) RAD21 fold change relative to siCon samples at the 0h timepoint
681 in siCon, siNIPBL, siAQR and siNIPBL+siAQR. Data is from 2 biological replicates and
682 is represented as mean +/- SEM.
683
684
685

686 **REFERENCES**

687 1. Leiserson, M. D. M. *et al.* Pan-cancer network analysis identifies combinations of rare
688 somatic mutations across pathways and protein complexes. *Nat. Genet.* **47,** 106–114
689 (2015).
690 2. Horsfield, J. A. *et al.* Cohesin-dependent regulation of Runx genes. *Development* **134,**
691 2639–2649 (2007).
692 3. Viny, A. D. & Levine, R. L. Cohesin mutations in myeloid malignancies made simple.
693 *Curr. Opin. Hematol.* **25,** 61–66 (2018).
694 4. Hadjur, S. *et al.* Cohesins form chromosomal cis-interactions at the developmentally
695 regulated IFNG locus. *Nature* **460,** 410–413 (2009).
696 5. Sofueva, S. *et al.* Cohesin-mediated interactions organize chromosomal domain
697 architecture. *EMBO J.* **32,** 3119–3129 (2013).
698 6. Zuin, J. *et al.* Cohesin and CTCF differentially affect chromatin architecture and gene
699 expression in human cells. *Proc. Natl. Acad. Sci. U.S.A.* **111,** 996–1001 (2014).
700 7. Kojic, A. *et al.* Distinct roles of cohesin-SA1 and cohesin-SA2 in 3D chromosome
701 organization. *Nature Publishing Group* **25,** 496–504 (2018).
702 8. Rao, S. S. P. *et al.* Cohesin Loss Eliminates All Loop Domains. *Cell* **171,** 305–309.e24
703 (2017).
704 9. Wutz, G. *et al.* Topologically associating domains and chromatin loops depend on
705 cohesin and are regulated by CTCF, WAPL, and PDS5 proteins. *EMBO J.* **36,** 3573–
706 3599 (2017).
707 10. Fudenberg, G., Abdennur, N., Imakaev, M., Goloborodko, A. & Mirny, L. Emerging
708 Evidence of Chromosome Folding by Loop Extrusion. *bioRxiv* 1–24 (2018).
709 doi:10.1101/264648
710 11. Balbás-Martínez, C. *et al.* Recurrent inactivation of STAG2 in bladder cancer is not
711 associated with aneuploidy. *Nat. Genet.* **45,** 1464–1469 (2013).
712 12. Solomon, D. A. *et al.* Frequent truncating mutations of STAG2 in bladder cancer. *Nat.*
713 *Genet.* **45,** 1428–1430 (2013).
714 13. Murayama, Y. & Uhlmann, F. Biochemical reconstitution of topological DNA binding by
715 the cohesin ring. *Nature* **505,** 367–371 (2014).
716 14. Orgil, O. *et al.* A conserved domain in the scc3 subunit of cohesin mediates the
717 interaction with both mcd1 and the cohesin loader complex. *PLoS Genet.* **11,** e1005036
718 (2015).
719 15. Ciosk, R. *et al.* Cohesin's Binding to Chromosomes Depends on a Separate Complex
720 Consisting of Scc2 and Scc4 Proteins. *Molecular Cell* **5,** 243–254 (2000).
721 16. Li, Y. *et al.* Structural basis for Scc3-dependent cohesin recruitment to chromatin. *eLIFE*
722 **7,** 352 (2018).
723 17. Shi, Z., Gao, H., Bai, X.-C. & Yu, H. Cryo-EM structure of the human cohesin-NIPBL-
724 DNA complex. *Science* **368,** 1454–1459 (2020).
725 18. Higashi, T. L. *et al.* A Structure-Based Mechanism for DNA Entry into the Cohesin Ring.
726 *Molecular Cell* **79,** 917–933.e9 (2020).
727 19. Xiao, T., Wallace, J. & Felsenfeld, G. Specific sites in the C terminus of CTCF interact
728 with the SA2 subunit of the cohesin complex and are required for cohesin-dependent
729 insulation activity. *Mol. Cell. Biol.* **31,** 2174–2183 (2011).
730 20. Saldaña-Meyer, R. *et al.* CTCF regulates the human p53 gene through direct interaction
731 with its natural antisense transcript, Wrap53. *Genes Dev.* **28,** 723–734 (2014).
732 21. Bisht, K. K., Daniloski, Z. & Smith, S. SA1 binds directly to DNA through its unique AT-
733 hook to promote sister chromatid cohesion at telomeres. *J. Cell. Sci.* **126,** 3493–3503
734 (2013).
735 22. Lin, J. *et al.* Functional interplay between SA1 and TRF1 in telomeric DNA binding and
736 DNA-DNA pairing. *Nucleic Acids Research* **44,** 6363–6376 (2016).
737 23. Countryman, P. *et al.* Cohesin SA2 is a sequence-independent DNA-binding protein that
738 recognizes DNA replication and repair intermediates. *J. Biol. Chem.* **293,** 1054–1069
739 (2018).
740 24. Murayama, Y., Samora, C. P., Kurokawa, Y., Iwasaki, H. & Uhlmann, F. Establishment
741 of DNA-DNA Interactions by the Cohesin Ring. *Cell* 1–29 (2018).

doi:10.1016/j.cell.2017.12.021
25. Zheng, G., Kanchwala, M. & Xing, C. MCM2–7-dependent cohesin loading during S phase promotes sister-chromatid cohesion. *eLIFE* 1–25 (2018). doi:10.7554/eLife.33920.001
26. Natsume, T., Kiyomitsu, T., Saga, Y. & Kanemaki, M. T. Rapid Protein Depletion in Human Cells by Auxin-Inducible Degron Tagging with Short Homology Donors. *Cell Rep* **15,** 210–218 (2016).
27. Parelho, V. *et al.* Cohesins functionally associate with CTCF on mammalian chromosome arms. *Cell* **132,** 422–433 (2008).
28. Wendt, K. S. *et al.* Cohesin mediates transcriptional insulation by CCCTC-binding factor. *Nature* **451,** 796–801 (2008).
29. Roig, M. B. *et al.* Structure and function of cohesinâ€™s Scc3/SA regulatory subunit. *FEBS Letters* **588,** 3692–3702 (2014).
30. Hons, M. T. *et al.* Topology and structure of an engineered human cohesin complex bound to Pds5B. *Nature Communications* **7,** 1–11 (2017).
31. Kim, J.-S. *et al.* Systematic proteomics of endogenous human cohesin reveals an interaction with diverse splicing factors and RNA-binding proteins required for mitotic progression. *J. Biol. Chem.* **294,** 8760–8772 (2019).
32. Irimia, M. *et al.* A Highly Conserved Program of Neuronal Microexons Is Misregulated in Autistic Brains. *Cell* **159,** 1511–1523 (2014).
33. Santos-Pereira, J. M. & Aguilera, A. R loops: new modulators of genome dynamics and function. *Nat. Rev. Genet.* **16,** 583–597 (2015).
34. Cristini, A., Groh, M., Kristiansen, M. S. & Gromak, N. RNA/DNA Hybrid Interactome Identifies DXH9 as a Molecular Player in Transcriptional Termination and R-Loop-Associated DNA Damage. *Cell Rep* **23,** 1891–1905 (2018).
35. Wang, I. X. *et al.* Human proteins that interact with RNA/DNA hybrids. *Genome Res.* **28,** 1405–1414 (2018).
36. Sollier, J. *et al.* Transcription-coupled nucleotide excision repair factors promote R-loop-induced genome instability. *Molecular Cell* **56,** 777–785 (2014).
37. Skourti-Stathaki, K., Kamieniarz-Gdula, K. & Proudfoot, N. J. R-loops induce repressive chromatin marks over mammalian gene terminators. *Nature* **516,** 436–439 (2014).
38. Cerritelli, S. M. & Crouch, R. J. Ribonuclease H: the enzymes in eukaryotes. *FEBS J.* **276,** 1494–1505 (2009).
39. Kikuchi, S., Borek, D. M., Otwinowski, Z., Tomchick, D. R. & Yu, H. Crystal structure of the cohesin loader Scc2 and insight into cohesinopathy. *Proc. Natl. Acad. Sci. U.S.A.* **113,** 12444–12449 (2016).
40. Hara, K. *et al.* Structure of cohesin subcomplex pinpoints direct shugoshin-Wapl antagonism in centromeric cohesion. *Nature Publishing Group* **21,** 864–870 (2014).
41. Watrin, E. *et al.* Human Scc4 is required for cohesin binding to chromatin, sister-chromatid cohesion, and mitotic progression. *Curr. Biol.* **16,** 863–874 (2006).
42. Pan, H. *et al.* Cohesin SA1 and SA2 are RNA binding proteins that localize to RNA containing regions on DNA. *Nucleic Acids Research* **24,** 105–17 (2020).
43. Chao, W. C. H. *et al.* Structural Studies Reveal the Functional Modularity of the Scc2-Scc4 Cohesin Loader. *Cell Rep* **12,** 719–725 (2015).
44. Pezic, D. *et al.* The cohesin regulator Stag1 promotes cell plasticity through heterochromatin regulation. *bioRxiv* 1–60 (2021). doi:10.1101/2021.02.14.429938
45. Li, Y. *et al.* The structural basis for cohesin-CTCF-anchored loops. *Nature* **578,** 472–476 (2020).
46. Yao, H. *et al.* Mediation of CTCF transcriptional insulation by DEAD-box RNA-binding protein p68 and steroid receptor RNA activator SRA. *Genes Dev.* **24,** 2543–2555 (2010).
47. García-Muse, T. & Aguilera, A. R Loops: From Physiological to Pathological Roles. *Cell* 1–15 (2019). doi:10.1016/j.cell.2019.08.055
48. Misteli, T. Beyond the Sequence: Cellular Organization of Genome Function. *Cell* **128,** 787–800 (2007).
49. Nozawa, R.-S. *et al.* SAF-A Regulates Interphase Chromosome Structure through Oligomerization with Chromatin- Associated RNAs. *Cell* **169,** 1214–1227.e18 (2017).
50. Huo, X. *et al.* The Nuclear Matrix Protein SAFB Cooperates with Major Satellite RNAs to

800 Stabilize Heterochromatin Architecture Partially through Phase Separation. *Molecular*
801 *Cell* **77,** 368–383.e7 (2020).
802 51. Barrington, C., Georgopoulou, D., Nature, D. P.2019. Enhancer accessibility and CTCF
803 occupancy underlie asymmetric TAD architecture and cell type specific genome
804 topology. *Nat Communications.* doi:10.1038/s41467-019-10725-9
805 52. Cox, J. & Mann, M. MaxQuant enables high peptide identification rates, individualized
806 p.p.b.-range mass accuracies and proteome-wide protein quantification. *Nat Biotechnol*
807 **26,** 1367–1372 (2008).
808 53. Choi, M. *et al.* MSstats: an R package for statistical analysis of quantitative mass
809 spectrometry-based proteomic experiments. *Bioinformatics* **30,** 2524–2526 (2014).
810 54. Beltran, M. *et al.* The interaction of PRC2 with RNA or chromatin is mutually
811 antagonistic. *Genome Res.* **26,** 896–907 (2016).
812

METHODS

Cell culture and IAA-mediated degradation of Rad21.

HCT116 cells with engineered RAD21-miniAID-mClover (RAD21mAC), or OsTIR1-only, or both (RAD21mAC-OsTIR) were obtained from Masato T. Kanemaki. The cells were maintained in McCoy's 5A medium with Glutamax (Thermo Fisher Scientific) supplemented with 10% Heat-inactivated FBS (Gibco), 700μg/ml Geneticin, 100μg/ml Hygromycin B Gold and 100μg/ml Puromycin as described in (Natsume). We clonally selected the RAD21mAC-OsTIR cells by sorting green fluorescence positive single cells on a FACS Aria Fusion cell sorter (BD Bioscience). Single cells were individually seeded into one well of a 96-well plate, expanded for 10 days into 6cm culture dishes and selected with Geneticin, Hygromycin B Gold and Puromycin as indicated above in McCoy's medium for another 10 days. Each clone was assessed for efficiency of Rad21 degradation using FACS analysis and western blotting (WB) using mClover, mAID and OsTIR antibodies. Two clones (H2 and H11) were taken forward and used throughout this study. To deplete RAD21, RAD21mAC-OsTIR cells were grown in adherent conditions for 3 days and treated with 500 μM Indole-3-acetic acid (IAA, Auxin, diluted in ethanol) for 4 hours. For IAA withdrawal, IAA treated cells were washed with PBS and replaced with fresh supplemented McCoy's medium for another 4 hours. Cells were washed twice with ice-cold PBS before being harvested for later experimental procedures.

siRNA-mediated knockdowns.

For siRNA transfections, RAD21^{mAC}-OsTIR cells were reverse transfected with scramble siRNA (siCon) or siRNAs targeting SA1, SA2, NIPBL, or AQR (Dharmacon, Horizon Discovery). A final concentration of 10 nM of siSA1, siSA2, or siNIPBL or 5 nM of siAQR was reverse transfected into the cells using Lipofectamine RNAiMAX reagent (Invitrogen), as per the manufacturer's instructions. Cells were plated at a density of 1 – 1.25 x 10^6 cells per 10 cm dish and harvested 72hrs post-transfection, at a confluency of ~70%. The Lipofectamine-containing media was replaced with fresh media 12-16 hrs post-transfection to avoid toxicity. For Figure 5f/g, incubation time was reduced to 48 hrs. To account for the reduced growth time, cells were plated at a density of 2-3 x 10^6 cells per 10 cm dish. Here siCon- and siNIPBL-transfected cells were plated at a lower cell number than siAQR-transfected cells to ensure equalised confluence (~70%) at the time of collection. When IAA-treatment was combined with siRNA mediated KD, the IAA was added at the end of the normal KD condition so that total KD time was not changed compared to UT cells. For esiRNA treatment, RAD21^{mAC}-OsTIR cells were reverse-transfected with 20 μM FLUC control esiRNA or esiRNA custom designed to SA1 exon31 or SA2 exon32 (MISSION® siRNA, Sigma Aldrich) using RNAiMAX (Invitrogen). Cells were incubated in transfection mixture for 7-8 hours before being replaced with fresh supplemented McCoy's medium and left for

854 another 40h until harvest. Efficiency of KD was assessed by WB. siRNA information
855 can be found in Table 1.
856
857 **Immunofluorescence**
858 Cells were adhered onto poly L-lysine coated glass coverslips in 6 well
859 culture dishes and were washed twice with ice-cold PBS before IF procedures. For
860 RAD21-depletion analysis, cells were fixed for 10 mins at room temperature with 3.7%
861 paraformaldehyde (Alfa Aesar) in PBS, washed 3 times with PBS and
862 then permeabilized at room temperature for 10 mins with 0.25% Triton X-100 in PBS
863 (Sigma Aldrich). For R-loop imaging, cells were fixed and permeabilised with ice-cold
864 ultra-pure methanol (Sigma Aldrich) for 10 mins at -20°C. After 3 washes with PBS,
865 cells were blocked for 45 mins at room temperature with 10% FCS-PBS. For
866 RNASEH1 enzyme treatment, cells were incubated with blocking solution
867 supplemented with 1x RNASEH1 reaction buffer alone (50 mM Tris-HCl, 75 mM KCl,
868 3 mM $MgCl_2$, 10 mM DTT) or 5 units of RNASEH1 enzyme (M0297, New England
869 Biolabs) for 30 mins at 37 °C, PBS-washed twice, before blocking. Cells were washed
870 twice with PBS before incubation with primary antibodies diluted in 5% FCS-PBS at 4
871 °C overnight. Anti-SA1, anti-SA2 and anti-AQR were used at 1:3000 dilutions; anti-
872 CTCF was used at 1:2500 dilution; anti-s9.6 was used at 1:1000 dilution; anti-V5 was
873 used at 1:1000. After 4 washes with PBS, cells were incubated with secondary
874 antibodies (donkey anti-Goat AF555 or AF647 for SA1/2 used at 1:3000; donkey anti-
875 Rabbit AF647 for CTCF used at 1:2500; donkey anti-Mouse AF555 for s9.6 used at
876 1:2000; donkey anti-Rabbit AF647 for AQR used at 1:3000; donkey anti-Rabbit AF488
877 for V5 used at 1:2000)) in 5% FCS-PBS for 1 hour at room temperature, and washed
878 4 times with PBS before being mounted onto glass slides with ProLong™ Diamond
879 Antifade Mountant with DAPI (Thermo Fisher Scientific) to stabilise overnight in dark
880 before imaging. See Table 2 for details of where antibodies were purchased.
881 Imaging was performed on Zeiss LSM confocal microscopes using 63x/1.40
882 NA Oil Plan-Apochromat objective lens (Carl Zeiss, Inc.). Images were captured as z-
883 stacks and under consistent digital gain, laser intensity and resolution for each
884 experiment. Numerical analysis was carried out using Imaris software (Oxford
885 Instruments, version 9.5.1) and representative images are shown as maximum z-
886 projected views generated using Fiji Image J. In brief, z-stack images were imported
887 into Imaris, cells were identified using DAPI and only those located 1 μm away from
888 image boundary and sized between 120-800 μm^3 were selected. A seed-split function
889 of 7.5um was used to separate closely situated cells. Fluorescence intensities of
890 individual DAPI-selections in each channel were determined by Imaris and exported
891 into Excel for further analysis. Distribution plots were generated from >50 cells of each
892 replicate with 3 biological replicates per experiment. Student's *t*-test was performed
893 between control and experimental conditions and statistical significance was
894 determined by detecting the difference between means (unequal variance, two-tailed).

895 Significance is denoted as p>0.05 = not significant (ns), p≤0.05 = *, p≤0.01 = **,
896 p≤0.001 = *** and p≤0.0001 = ****.
897
898 **Chromatin Fractionation and colmmunoprecipitation.**
899 Cells were washed twice with ice-cold PBS (Sigma Aldrich) and lysed in Buffer A (10
900 mM HEPES, 10mM KCl, 1.5 mM MgCl2, 0.34 M Sucrose, 10% Glycerol, 1mM DTT,
901 1mM PMSF/Pefabloc, protease inhibitor), supplemented with 0.1% T-X100, for 10 min
902 on ice. Lysed cells were collected by scraping. Nuclei and cytoplasmic
903 material was separated by centrifugation for 4 min at 1300 g at 4oC. The supernatant
904 was collected as the cytoplasmic fraction and cleared of any insoluble material with
905 further centrifugation for 15 min at 20,000 g at 4oC. The nuclear pellet was washed
906 once with buffer A before lysis in buffer B (3mM EDTA, 0.2mM EGTA, 1mM DTT, 1mM
907 PMSF/Pefabloc, protease inhibitor) with rotation for 30 min at 4oC. Insoluble nuclear
908 material was spun down for 4 min at 1700 g at 4oC and the supernatant taken as
909 nuclear soluble fraction. The insoluble material was wash once with buffer B and then
910 resuspended in high-salt chromatin solubilization buffer (50mM Tris-HCl pH 7.5, 1.5
911 mM MgCl2, 500mM KCl, 1mM EDTA, 20% Glycerol, 0.1% NP-40, 1mM
912 PMSF/Pefabloc, protease inhibitor). The lysate was vortexed for 2 min to aid
913 solubilization. Nucleic acids were digested with 85U benzonase (Sigma-Aldrich) per
914 100 x 106 cells, with incubation for 10 min at 37oC and 20 min at 4oC. Chromatin was
915 further solubilized with ultra-sonication for 3 x 10 sec at an amplitude of 30. The lysate
916 was diluted to 200 mM KCl and insoluble material was removed by centrifugation at
917 15,000 RPM for 30 min at 4oC.
918 For coIP, antibodies were bound to Dynabead Protein A/G beads
919 (ThermoFisher Scientific) for 10 min at room temperature and ~ 5 hr at 4oC. For mock
920 IgG IPs, beads were incubated with serum from the same host type as the antibody of
921 interest. 1mg of chromatin extract was incubated with the antibody-bead conjugate per
922 IP for approximately 16 hr at 4oC. IPs were washed x5 with IP buffer (200mM
923 chromatin solubilization buffer) and eluted by boiling in either 2x Laemmeli sample
924 buffer (BioRad) or 4x NuPAGE LDS sample buffer (ThermoFisher Scientific). Proteins
925 ≤ 250 kDa were separated by SDS-PAGE electrophoresis using 4–20% Mini-
926 PROTEAN® TGX™ Precast Protein Gels (BioRad) and transferred to Immobilon-P
927 PVDF Membrane (Merck Millipore) for detection. Proteins ≥ 250 kDa were separated
928 by SDS-PAGE electrophoresis using Invitrogen NuPAGE 3-8% Tris-Acetate precast
929 protein gels. Transfer was extended to overnight with low voltage (20V) to aid in
930 transfer of the high-molecular weight proteins. Membranes were incubated in primary
931 antibody solution overnight at 4oC and images were detected using chemiluminescent
932 fluorescence. Densitometry was carried out using ImageStudio Lite software with
933 statistical significance calculated by unpaired t test, unless otherwise specified. Fold
934 enrichment quantifications were performed by first normalising the raw densitometry
935 value to its corresponding Histone H3 quantification and the comparing between the
936 samples indicated. See Table 2 for details of antibodies.

937
938 **S9.6 IP and Dot Blot.**
939 Cells were fractioned and processed for S9.6 IP as described above, with the following
940 modifications. To avoid digestion of RNA:DNA hybrids, samples were not treated
941 with benzonase during chromatin solubilization and sonication was carried out for 10
942 min (Diagenode Biorupter) as in [34]. Where indicated, chromatin samples were treated
943 with Ribonuclease H enzyme (NEB) overnight at 37°C to digest RNA:DNA hybrids in
944 the extract. To avoid detection of single-stranded RNA by the S9.6 antibody, all S9.6
945 IP samples were pre-treated with Purelink RNase A (Thermo Fisher Scientific) at
946 0.25ug/1mg chromatin extract for 1 hr 30 min at 4°C. The reaction was stopped with
947 addition of 143U Invitrogen SUPERase•In RNase Inhibitor (Thermo Fisher
948 Scientific). RNA:DNA hybrid levels were assessed in chromatin samples by dot blot.
949 Specifically, the chromatin lysate was directly wicked
950 onto Amersham Protran nitrocellulose membrane (Merck) by pipetting small volumes
951 above the membrane. Membranes were blocked in 5% (w/v) non-fat dry milk in PBS-
952 0.1% Tween and incubated with S9.6 antibody overnight as for standard western blot.
953 As above, detection was carried out using chemiluminescent fluorescence. RNase A-
954 mediated digestion of RNA:DNA hybrids was performed using a non-ssRNA-specific
955 enzyme (Thermo Scientific) at 1.5ug/25ug chromatin extract at 37°C.
956
957 **ChIP-sequencing, library preparation and analysis.**
958 ChIP lysates were prepared from RAD21^{mAC} cells treated with ethanol or IAA for
959 4hrs in two biological replicates. Formaldehyde (1%) was added to the culture
960 medium for 10min at room temperature. Fixation was blocked with 0.125M glycine and
961 cells were washed in cold PBS. Nuclear extracts were prepared by douncing (20
962 strokes, medium pestle) in swelling buffer (25 mM HEPES pH8, 1.5 mM MgCl2, 10mM
963 KCL, 0.1% NP40, 1 mM DTT and protease inhibitors) and centrifuged for 5min at
964 2000rpm at 4C. Nuclear pellets were resuspended in Sucrose buffer I
965 (15mM Hepes pH 8, 340 mM Sucrose, 60mM KCL, 2mM EDTA, 0.5 mM EGTA, 0.5%
966 BSA, 0.5 mM DTT and protease inhibitors) and dounced again with 20 strokes. The
967 lysate was carefully laid on top of an equal volume of Sucrose buffer
968 II (15mM Hepes pH 8, 30% Sucrose, 60mM KCL, 2mM EDTA, 0.5 mM EGTA, 0.5 mM
969 DTT and protease inhibitors) and centrifuged for 15min at 4000rpm at 4C. Nuclei were
970 washed twice to remove cytoplasmic proteins, centrifuged and the pellet was
971 resuspended in Sonication/RIPA buffer (50mM Tris, pH 8.0, 140 mM NaCl, 1 mM
972 EDTA, 1% Triton X-100, 0.1% Na-deoxycholate, 0.1% SDS and protease inhibitors) at
973 a concentration of 5 x10^6 nuclei in 130µl buffer. This was transferred to a sonication
974 tube (AFA Fiber Pre-Slit Snap-Cap 6x16mm) and sonicated in a Covaris S2 (settings;
975 4 cycles of 60 seconds, 10% duty cycle, intensity: 5, 200 cycles per
976 burst). Soluable chromatin was in the range of 200 - 400 bp. Triton X100 was added
977 (final concentration 1%) to the sonicated chromatin and moved to a low-retention

978 tube (Eppendorf) before centrifugation at 14,000 rpm for 15min at 4C and pellets were
979 discarded. 1/100th of the chromatin lysate was retained as the Input sample.
980 For Immunoprecipitation, 200ug chromatin aliquots/IP were precleared with a
981 slurry of Protein A/G (50:50) (Dynabeads) an incubated for 4hr at 4C. Meanwhile,
982 washed Protein A/G beads (40ul per IP) were mixed with primary antibodies and
983 incubated for 4hrs at 4C. The following amounts of antibodies were used: anti-
984 CTCF, 5ug/ChIP; anti-SA1, 15ug/ChIP; anti-SA2, 10ug of the mixed antibody
985 pack/ChIP; anti-Smc3, 5ug/ChIP and anti-IgG, 10ug/ChIP. See Table 2 for information
986 about the antibodies. Washed, pre-bound Protein A/G beads+antibody were mixed
987 with pre-cleared chromatin lysates and incubated overnight with rotation at 4C. The
988 next day, the supernatant was removed and the beads were washed 9 times with
989 increasing salt concentrations. Protein-DNA crosslinks were reversed in ChIP elution
990 buffer (1% SDS, 5 mM EDTA, 10 mM Tris HCl pH 8) + 2.5 ul of Proteinse K and
991 incubated for 1 hour at 55°C and overnight at 65°C. Samples were phenol–chloroform
992 extracted, resuspended in TE buffer and assessed by qPCR as a quality
993 control. Libraries were prepared from 5-10ng of purified DNA, depending on
994 availability of material, using NEBNext Ultra II DNA Library Prep Kit for Illumina kit and
995 using NEBNext Multiplex Oligos for Illumina (Index Primers Set 2) according to
996 manufacturer's instructions using 6-8 cycles of PCR. ChIP-seq libraries from one
997 biological set (all ChIP libraries for both ethanol and
998 IAA) were multiplexed and sequenced on the Illumina HiSeq2500 platform, 80bp
999 single-end reads. Each biological set was sequenced on a separate run.
1000 Quality control of reads was preformed using FASTQC. Reads were aligned to
1001 the hg19 reference genome using Bowtie with 3 mismatches. Only replicate 1 of the
1002 SA1 librraye was used. PCR duplicates were detected and removed using
1003 SAMTOOLS. Bam files were imported into MISHA (v 3.5.6) and peaks were identified
1004 using a 0.995 percentile. Peaks that overlapped in both replicates were
1005 retained. Correlation plots of peaks across the genome from different ChIP libraries
1006 were compared with log-transformed percentiles plotted as a smoothed scatter plot.
1007 Comparison of peaks at regions of interest were carried out using deepTools (Version
1008 3.1.0-2 REF). For input into deepTools, peak data was converted to bigwig format,
1009 with a bin size of 500, using the UCSC bedGraphtoBigWig package. The signal matrix
1010 was calculated for a window 2,000 bp up- and down-stream of the region of interest,
1011 missing data was treated as zero, and all other parameters were as default. Heatmaps
1012 were generated within deepTools, with parameters as default.
1013
1014 **Hi-C data and contact hotspots analysis.**
1015 Generating hotspots - Previously published Hi-C datasets derived from
1016 RAD21^{mAC} cells treated with ethanol or IAA [8] were analyzed as previously described
1017 [51]. Custom R scripts were written to identify Hi-C hotspots, i.e. regions of Hi-C maps
1018 with high contact frequency. To begin, for each chromosome, all contacts were
1019 extracted and subsetted for only high scoring (>=60) contacts between a band of 10e3

– 70e6. Using KNN, for each high scoring contact, the 250 nearest neighbour contacts were identified and subset for only the high-scoring neighbours. This created a list of high scoring neighbours for each high scoring contact, where the first neighbour is the contact itself with a distance of 0. This allowed the neighbour information to be converted into edge information, thereby allowing high score fend contacts to be grouped into cluster hotspots using the R package 'igraph'. Hotspots that contained less than the minimum number of high scoring fends (<100) were removed. The output list of hotspots were represented as 2D intervals which contained high scoring contacts. In total, 5539 hotspots were identified in EtOH and 759 in IAA Hi-C data.

Creating aggregate plots - To calculate and visualise the contact enrichment at hotspots in the EtOH and IAA Hi-C, we used the R package 'shaman'. Firstly, we used the function 'shaman_generate_feature_grid' to calculate the enrichment profile at EtOH and IAA hotspots. Using the weighted centre for each hotspot, represented as a 2D interval we used the function to build grids for the EtOH and IAA hotspots in the HiC data at 3 specific bands, 100k – 1MB, 1MB – 5MB, 5MB – 10MB. A range of 250kb was visualised around the weighted centre. The grid was built by taking all combinations interval1 and interval2 of the EtOH and IAA hotspot centres, with each combination termed a 'window'. Hotspots were not filtered for size or shape. A score threshold of 60 was used to focus on enriched pairs, those windows that did not contain at least one point with a score of 60 were discarded. Each window was then split into 1000nt bins and the windows were summed together to generate a grid containing the observed and expected contacts. We visualised the grid using 'shaman_plot_feature_grid' using 'enrichment' mode and a plot_resolution value of 6000, due to the large range being visualised.

STORM – Immunolabelling and imaging.

Two clones of RAD21^{mAC}-OsTIR cells were seeded at a density of 30,000 cells per well per 400ul) onto poly-L-lysine coated 8-well chamber slides (Lab-Tek™ 155411) overnight. Each clone was treated with either ethanol (EtOH) or Auxin (IAA) for 4hr and then fixed with PFA 4% (Alfa Aesar) for 10 min at room temperature and rinsed with PBS three times for 5 min each. The cells were shipped to the Cosma Lab after fixation for STORM processing and imaging. Cells were permeabilized with 0.3% Triton X-100 in PBS and blocked in blocking buffer (10% BSA – 0.01 % Triton X-100 in PBS) for one hour at room temperature. Cells were incubated with primary antibodies (see Table 2) in blocking buffer at 1:50 dilution. Cells were washed three times for 5 min each with wash buffer (2% BSA – 0.01 % Triton X-100 in PBS) and incubated in secondary antibody. For STORM imaging, home-made (Bates et al., 2007) dye pair labeled secondary antibodies were added at a 1:50 dilution in blocking buffer and were incubated for 45 min at room temperature. Cells were washed three times for 5 min each with wash buffer.

1061 STORM imaging was performed on an N-STORM 4.0 microscope (Nikon)
1062 equipped with a CFI HP Apochromat TIRF 100x 1.49 oil objective and an iXon Ultra
1063 897 camera (Andor) and using Highly Inclined and Laminated Optical sheet
1064 illumination (HILO). Dual color STORM imaging was performed with a double activator
1065 and single reporter strategy by combining AF405_AF647 anti-Goat secondary with
1066 Cy3_AF647 anti-Rabbit secondary antibodies. Sequential imaging acquisition was
1067 performed (1 frame of 405 nm activation followed by 3 frames of 647 nm reporter and
1068 1 frame of 560 nm activation followed by 3 frames of 647 nm reporter) with
1069 10 ms exposure time for 120000 frames. 647 nm laser was used at constant ~2
1070 kW/cm^2 power density and 405 nm and 560 nm laser powers were gradually increased
1071 over the imaging. Imaging buffer composition for STORM imaging was 100 mM
1072 Cysteamine MEA (Sigma-Aldrich, #30070) - 5% Glucose (Sigma-Aldrich, #G8270) –
1073 1% Glox Solution (0.5 mg/ml glucose oxidase, 40 mg/ml catalase (Sigma-Aldrich,
1074 #G2133 and #C100)) in PBS.
1075
1076 **STORM imaging analysis and quantifications.**
1077 STORM images were analyzed and rendered in Insight3 (kind gift of Bo Huang, UCSF)
1078 as previously described (Bates et al., 2007; Rust et al., 2006). Localizations were
1079 identified based on a threshold and fit to a simple Gaussian to determine the x and y
1080 positions. Cluster analysis of CTCF, SA1 and SA2 STORM signal was performed as
1081 previously described (Ricci et al., 2015) to obtain cluster size and positions and to
1082 measure Nearest Neighbour distributions (NND) between clusters of the same protein
1083 in individual nuclei. NND between clusters' centroids of two different proteins
1084 (i.e. CTCF-SA1 and CTCF-SA2) was calculated by knnsearch.m Matlab function and
1085 the NND histogram of experimental data was obtained by considering all the NNDs of
1086 individual nuclei (histogram bin, from 0 to 500 nm, 5 nm steps). Simulated NNDs
1087 recapitulating random spatial distribution of cluster centroids were first obtained for
1088 each nucleus separately and then merged to calculate the simulated NND histogram
1089 (histogram bin, from 0 to 500 nm, 5 nm steps). The difference plot reports the
1090 difference between experimental NND and simulated NND. Quantification and
1091 analysis of STORM images was performed in Matlab and statistical
1092 analysis was performed in Graphpad Prism (v7.0e). The type of statistical test is
1093 specified in each case. Statistical significance is represented as indicated above.
1094 Insight3 Software used for STORM image processing has been generated (Huang et
1095 al., 2008) and kindly provided by Dr Bo Huang (UCSF). Graphpad Prism software
1096 used for statistical analysis can be found at: https://www.graphpad.com/scientific-
1097 software/prism/ MatLab software used for imaging data analysis can be found
1098 at: https://www.mathworks.com/products/matlab.html
1099
1100 **Mass spectrometry sample preparation and running**.
1101 SA1 immunoprecipitation samples were analysed by liquid chromatography–tandem
1102 mass spectrometry (LC-MS/MS). Three biological replicate experiments were carried

1103 out for MS and each included four samples, untreated (UT), treated with IAA for
1104 4hrs, siCon, or siSA1, generated as described above. A fourth technical replicate was
1105 also included for the UTR samples. Cells were fractionated to purify chromatin-bound
1106 proteins as above and immunoprecipitated with IgG- or SA1-bead
1107 conjugates. To maximise IP material for the MS, the antibody amount was increased
1108 to 15ug and the chromatin amount was increased to 2mg.
1109 The IP eluates were loaded into a pre-cast SDS-PAGE gel (4–20% Mini-
1110 PROTEAN® TGX™ Precast Protein Gel, 10-well, 50 μL) and proteins were run
1111 approximately 1 cm to prevent protein separation. Protein bands were excised and
1112 diced, and proteins were reduced with 5 mM TCEP in 50 mM triethylammonium
1113 bicarbonate (TEAB) at 37°C for 20 min, alkylated with 10 mM 2-chloroacetamide in 50
1114 mM TEAB at ambient temperature for 20 min in the dark. Proteins were then digested
1115 with 150ng trypsin, at 37°C for 3 h followed by a second trypsin addition for 4 h, then
1116 overnight at room temperature. After digestion, peptides were extracted with
1117 acetonitrile and 50 mM TEAB washes. Samples were evaporated to dryness at 30°C
1118 and resolubilised in 0.1% formic acid.
1119 nLC-MS/MS was performed on a Q Exactive Orbitrap Plus interfaced to a
1120 NANOSPRAY FLEX ion source and coupled to an Easy-nLC 1200 (Thermo Scientific).
1121 25% (first, second and fourth biological replicate) or 50% (third biological replicate) of
1122 each sample was loaded as 5 or 10 μL injections. Peptides were separated on a 27cm
1123 fused silica emitter, 75 µm diameter, packed in-house with Reprosil-Pur 200 C18-AQ,
1124 2.4 µm resin (Dr. Maisch) using a linear gradient from 5% to 30% acetonitrile/ 0.1%
1125 formic acid over 60 min, at a flow rate of 250 nL/min. Peptides were ionised by
1126 electrospray ionisation using 1.8 kV applied immediately prior to the analytical column
1127 via a microtee built into the nanospray source with the ion transfer tube heated to
1128 320°C and the S-lens set to 60%. Precursor ions were measured in a data-dependent
1129 mode in the orbitrap analyser at a resolution of 70,000 and a target value of 3e6 ions.
1130 The ten most intense ions from each MS1 scan were isolated, fragmented in the HCD
1131 cell, and measured in the orbitrap at a resolution of 17,500.
1132
1133 **Mass spectrometry analysis**
1134 Raw data was analysed with MaxQuant [52] version 1.5.5.1 where they were searched
1135 against the human UniProtKB database using default settings
1136 (http://www.uniprot.org/). Carbamidomethylation of cysteines was set as fixed
1137 modification, and oxidation of methionines and acetylation at protein N-termini were
1138 set as variable modifications. Enzyme specificity was set to trypsin with maximally 2
1139 missed cleavages allowed. To ensure high confidence identifications, PSMs, peptides,
1140 and proteins were filtered at a less than 1% false discovery rate (FDR). Label-free
1141 quantification in MaxQuant was used with LFQ minimum ratio count set to 2 with
1142 'FastLFQ' (LFQ minimum number of neighbours = 3, and LFQ average number of
1143 neighbours = 6) and 'Skip normalisation' selected. In Advanced identifications,
1144 'Second peptides' was selected and the 'match between runs' feature was not

1145 selected. Statistical protein quantification analysis was done in MSstats [53](version
1146 3.14.0) run through RStudio. Contaminants and reverse sequences were removed
1147 and data was log2 transformed. To find differential abundant proteins across
1148 conditions, paired significance analysis consisting of fitting a statistical model and
1149 performing model-based comparison of conditions. The group comparison function
1150 was employed to test for differential abundance between conditions. Unadjusted p-
1151 values were used to rank the testing results and to define regulated proteins between
1152 groups.
1153 Proteins with peptides discovered in the IgG samples were disregarded from
1154 downstream analyses. Significantly depleted/enriched proteins were considered with
1155 an absolute log2foldchange > 0.58 (1.5-fold change) and a p-value < 0.1. SA1
1156 interactome analysis was performed in STRING. The network was generated as a full
1157 STRING network with a minimum interaction score of 0.7 required. Over-enrichment
1158 of GO biological process and molecular function terms was calculated with the human
1159 genome as background. Network analysis of the SA1 interactome in IAA-treated
1160 samples was generated from the significantly depleted/enriched proteins, with a
1161 minimum interaction score of 0.4 required. Two conditions for functional enrichments
1162 were considered; i) enrichment was calculated with the human genome as background
1163 to determine the full SA1 interactome in the absence of cohesin, compared to the
1164 genome, and ii) enrichment was calculated with the untreated SA1 interactome as
1165 background, to determine the statistical effect of cohesin loss of the SA1 interactome
1166 itself. The network developed in i) was manually rearranged in Cytoscape for visual
1167 clarity, enriched categories were visualized using the STRING pie chart function and
1168 half of the proteins within each category were subset from the network based on
1169 pvalue change between UTR and IAA samples.
1170 Over-enrichment of the s9.6 interactome was calculated separately using the
1171 hypergeometric distribution for comparison with [34,35]. Significance was calculated
1172 using the dhyper function in R and multiple testing was corrected for using the p.adjust
1173 Benjamini & Hochberg method. To compare with a minimal background protein list,
1174 http://www.humanproteomemap.org was analysed on the Expression Atlas database
1175 to determine a list of proteins expressed in one or more of three tissue types
1176 corresponding to the cell types used across the different studies.
1177
1178
1179 **SLiMSearch analysis**
1180 The SLiMSearch tool http://slim.icr.ac.uk/slimsearch/, with default parameters was
1181 used to search the human proteome for additional proteins that contained the FGF-
1182 like motif determined in [16] to predict binding to SA proteins. The motif was input as
1183 [PFCAVIYL][FY][GDEN]F.{0,1}[DANE].{0,1}[DE]. Along with CTCF, four proteins
1184 found to contain the FGF-like motif, CHD6, MCM3, HNRNPUL2 and ESYT2 were
1185 validated for interaction with SA.
1186

1187

1188 **CLIP and iCLIP**

1189 Crosslinking immunoprecipitation (CLIP) was performed as previously described[54].
1190 Briefly, mESC or HCT116 cells were irradiated with 0.2 J/cm2 of 254 nm UV light in a
1191 Stratalinker 2400 (Stratagene). Cells were lysed in 1 ml of lysis buffer with Complete
1192 protease inhibitor (Roche). Lysates were passed through a 27 G needle, 1.6 U DNase
1193 Turbo (Thermofisher) per 10^6 cells and 0.8 (low) or 8 U (high) U RNase I (Ambion) per
1194 10^6 cells added, and incubated in a thermomixer at 37°C and 1100 rpm for 3 minutes.
1195 Lysates were then cleared by centrifugation and using Proteus clarification spin
1196 column, according to the manufacturer's instructions. Endogenous SA1 and SA2 were
1197 immunoprecipitated with 10 µg SA1 and SA2 antibodies or non-specific IgG control
1198 (Sigma) conjugated to protein G dynabeads (Dynal) for 4 hrs at 4°C. Tagged SA2
1199 proteins were immunoprecipitated from HCT116 cells 40 hours after transfection with
1200 30 µl GFP-Trap beads. IPs were washed three times with high salt buffer (containing
1201 1M NaCl and 1M urea) and once with PNK buffer and RNA labelled with 8 µl
1202 radioactive ^{32}P-gamma-ATP (Hartmann Analytic) for 5 mins at 37°C. For RNaseH1
1203 treatment, YFP-SA2 samples were split and either treated with PNK buffer alone or
1204 PNK buffer containing 50 U RNaseH1 for 15 mins at 37°C. RNPs were eluted in LDS
1205 loading buffer (Invitrogen) and resolved on a 4-12% gradient NuPAGE Bis-Tris gel
1206 (Invitrogen) and transferred onto 0.2 µm diameter pore nitrocellulose membrane. After
1207 blocking with PBST+milk, membranes were washed and exposed overnight to
1208 phosphorimager screen (Fuji) and RNA-^{32}P visualized using a Typhoon
1209 phosphorimager (GE) and ImageQuant TL (GE). Membranes were then
1210 immunoblotted for SA1, SA2, and RAD21 and visualized using an ImageQuantLAS
1211 4000 imager (GE). See Table 2 for details on antibodies.

1212

1213 **GFP-TRAP + Cloning of STAG2 s/l and YFP constructs**.

1214 SA2 cDNAs were cloned directly from HCT116 cells by PCR using KAPA
1215 HiFi HotStart PCR kit (Roche) (Fwd: ATGATAGCAGCTCCAGAAAACCAACTG; Rev:
1216 TTAAAACATTGACACTCCAAGAACTGATTCATCC). Two major isoforms were
1217 detected, SA2$^{\Delta ex32}$ where exon32 has been spliced out and SA2^{+ex32} where exon
1218 32 has been spliced in. Both SA2 cDNAs were cloned into pENTR/D vector
1219 (Invitrogen) and then into an N-terminal YFP-tagged Gateway cloning vector (a kind
1220 gift from Endre Kiss-Toth, University of Sheffield). Sequences were confirmed by
1221 restriction enzyme digestion and Sanger sequencing. Recombinant YFP-SA2$^{\Delta ex32}$ or
1222 YFP-SA2^{+ex32} were transfected into adherent HCT116 cells for 40 hours before being
1223 harvested. Cells were lysed, fractionated and sonicated following the same protocol
1224 for chromatin fractionation with the variation of chromatin solubilisation in NaCl IP
1225 buffer (50mM Tris-HCL pH 7.5, 150mM NaCl, 1mM EDTA, 0.1% NP-40, 20% Glycerol,
1226 1mM DTT). 1mg chromatin lysate was pre-cleared with a 50:50 mixture of protein A/G
1227 magnetic beads and GFP-Trap (Chromotek, gtd-20) was pre-blocked with 1mg/mL
1228 ultra-pure BSA (AM2616, Invitrogen) for 2h at 4°C. After blocking, GFP-Trap was

1229 washed twice with NaCl IP buffer and added to pre-cleared lysates to
1230 immunoprecipitate proteins for 1h at 4°C. Samples were washed in NaCl IP buffer and
1231 eluted in 2x Laemmli buffer (Bio-Rad). Proteins were separated by SDS-PAGE on a
1232 4-20% gradient mini-PROTEAN® Precast Gel (Bio-Rad) and transferred onto PVDF
1233 membrane for visualization.
1234
1235 **VAST-TOOLS**
1236 VAST-TOOLS was used to generate Percent Spliced In (PSI) scores, a statistic which
1237 represents how often a particular exon is spliced into a transcript using the ratio
1238 between reads which include and exclude said exon. Paired-end RNA-seq datasets
1239 were submitted to VAST-TOOLS (v2.1.3) using the Mmu genome (Tapial J et al, Gen
1240 Res 2017). Briefly, reads are split into 50nt words with a 25nt sliding window. The 50nt
1241 words are aligned to a reference genome using Bowtie to obtain unmapped reads.
1242 These unmapped reads are then aligned to a set of predefined exon-exon junction
1243 (EJJ) libraries allowing for the quantification of alternative exon events. The output
1244 was further interrogated using a script which searches all hypothetical EEJ
1245 combinations between potential donors and acceptors within Stag1. PSI scores could
1246 be obtained providing there was at least a single read within the RNAseq data that
1247 supported the event, although we only considered events supported by a minimum
1248 of 50 reads. Calculated PSI values for each alternatively spliced exon (and shown in
1249 Fig 3d), as well as the average PSI reported in the text are shown below. See
1250 Table 3 for names of published datasets used in this analysis.
1251

Dataset	**SA2 e32 PSI**	**Reads across junction**	**SA1 e31 PSI**	**Reads across junction**
ENCODE HCT	21.92	202.98	98.99	588
Zuo HCT	19.18	94.75	97.91	278.06
ENCODE HeLa	19.95	90.57	96.36	156.1
AVG	**20.35**		**97.75**	

1252
1253

1254 **Table 1. siRNAs used in this study.**

siRNA name	Company	Target	Catalogue no.	custom siRNA sequence
si scramble control	Dharmacon	Smartpool	D-001810-10-05	
siSA1	Dharmacon	Smartpool	L-010638-01-0010	
siSA2	Dharmacon	Smartpool	L-021351-00-0010	
siNIPBL	Dharmacon	Smartpool	L-012980-00-0010	
siAQR	Dharmacon	Smartpool	L-022214-01-0005	
siControl (scramble)	Dharmacon	Smartpool	D-001810-10-20	
esi control	Sigma	Luciferase	EHUFLUC	
esi SA1	Sigma	exon 31	custom esiRNA	TCCTCAGATGCAGATCTCTTGGTTAGGCC AGCCGAAGTTAGAAGACTTAAATCGGAAG GACAGAACAGGAATGAACTACATGAAAGTG AGAACTGGAGTGAGGCATGCTGT
esi SA2	Sigma	exon 32	custom esiRNA	CACGCAGGTAACATGGATGTTAGCTCAAAG ACAACAAGAGGAAGCAAGGCAACAGCAGG AGAGAGCAGCAATGAGCTATGTTAAACTG CGAACTAATCTTCAGCATGCCAT

1255
1256
1257 **Table 2. Antibodies used in this study.**

Protein	Company	Catalogue No.	Species	Figure References
SA1	Abcam	ab4455	mouse	1a, c, d, e, 2a, b, d, 3a, b, e, 4b, c, e, 5d
SA1	Abcam	ab4457	mouse	1i
SA2	Bethyl	A300-159	goat	1b, c, d, e, 2a, 3a, b, f, 4c, e, 5d
SA2	Bethyl, AbVantage Pack	A310-941A	goat	1i
CTCF	Diagenode	C15410210	rabbit	1c, d, i, 2a
CTCF	Cell signalling	2899s	rabbit	1a, e
Rad21	Abcam	ab992	rabbit	1c, d, i, 2a, d, 5b, d, f
GFP-TRAP	ChromoTek	gtd-20		1i, 3g
GFP	Invitrogen	A11122	rabbit	1a, e
mAID	MBL	M214-3	mouse	S1a
OsTIR	MBL	PD048	rabbit	S1a
Smc3	Abcam	ab9263	rabbit	1i
CHD6	Bethyl	A301-221A	rabbit	2a
Mcm3	Bethyl	A300-124A	goat	2a, 4b
HNRNPUL2	Abcam	ab195338	rabbit	2a
YTHDC1	Abcam	ab122340	rabbit	2d
FTSJ3	Bethyl	A304-199A-M	rabbit	2d
FANCI	Bethyl	A301-254A-M	rabbit	2d
TAF15	Abcam	ab134916	rabbit	2d
DHX9	Abcam	Ab26271	rabbit	2d, 4b
SSRP1	Abcam	ab26212	mouse	2d
INO80	Proteintech	18810-1-AP	rabbit	2d
ESYT2	Sigma-Aldrich	HPA002132	rabbit	2d
S9.6	Kerafast	ENH001	mouse	4b, c, e, 5f
RNase H2	Novus	NBP1-76981	rabbit	4b
AQR	Bethyl	A302-547A	rabbit	4b, e, 5f
Pol2	Covance	MMS-1289	mouse	4b
Mau2	Abcam	ab183033	rabbit	5b, d, f
NIPBL	Abbiotec	250133	rat	5b, d, f, S5
H3	Abcam	ab1791	rabbit	3e, f, 5b, d, f

Name (Secondary Abs)	Fluorophore	Company	Catalogue No.	Figure References
Donkey anti-Rabbit	Cy3_AF647	Home made from Jackson Immunoresearch IgG	Home made from 711-005-152	1e, S1
Donkey anti-Goat	AF405_AF647	Home made from Jackson Immunoresearch IgG	Home made from 705-005-147	1e, S1
Donkey anti-mouse	AF647	Invitrogen	A31570	1a, d, e
Donkey anti-rabbit	AF488	Invitrogen	A21206	1a, d, e
Donkey anti-rabbit	AF647	Invitrogen	A31573	1a, d, e
Donkey anti-goat	AF555	Invitrogen	A21432	1a, d, e
Donkey anti-goat	AF647	Invitrogen	A21447	1a, d, e

1258

1259 **Table 3. Published datasets used in this study.**

Accession no.	Analysis description	Publication DOI or Ref	Figure Reference
GSE104334	Long-range contact analysis of Hi-C datasets	10.1016/j.cell.2017.09.026	1i
GSE89729	Percent Spliced In (PSI) analysis of RNA-seq datasets	10.1172/jci.insight.91419	4d, “HCT Zuo”
GSM958749	Percent Spliced In (PSI) analysis of RNA-seq datasets	ENCODE HCT116 RNAseq	4d, “HCT ENCODE”
GSM958735	Percent Spliced In (PSI) analysis of RNA-seq datasets	ENCODE HeLa RNAseq	4d, “HeLa”

1260

Figure 1.

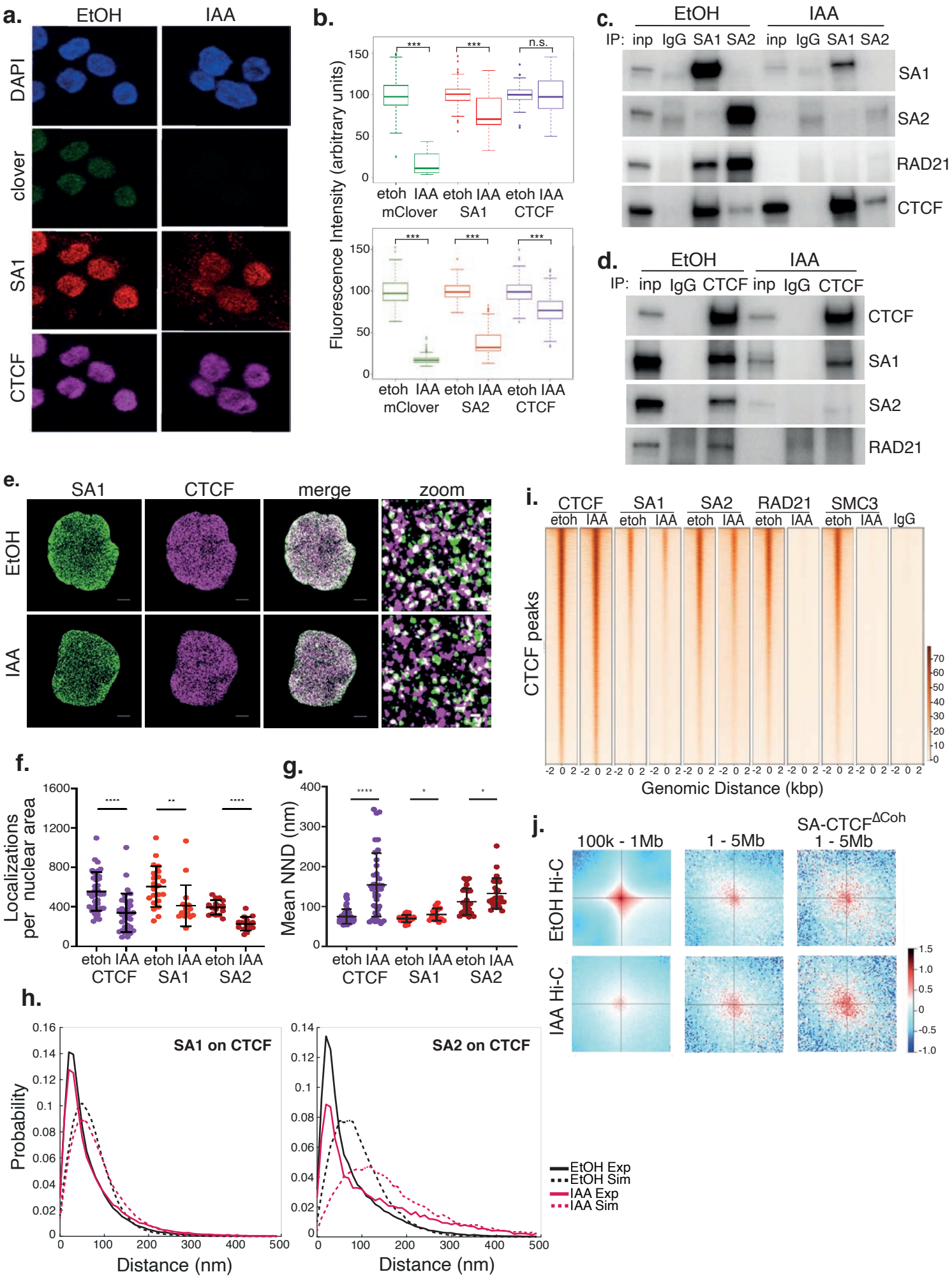
a.
EtOH
IAA
DAPI
clover
SA1
CTCF
b.
Fluorescence Intensity (arbitrary units)
etoh IAA etoh IAA etoh IAA
mClover SA1 CTCF
mClover SA2 CTCF
n.s.
c.
EtOH
IAA
IP: inp IgG SA1 SA2 inp IgG SA1 SA2
SA1
SA2
RAD21
CTCF
d.
IP: inp IgG CTCF inp IgG CTCF
e.
SA1
CTCF
merge
zoom
i.
CTCF SA1 SA2 RAD21 SMC3
etoh IAA etoh IAA etoh IAA etoh IAA etoh IAA IgG
CTCF peaks
Genomic Distance (kbp)
f.
Localizations per nuclear area
etoh IAA etoh IAA etoh IAA
CTCF SA1 SA2
g.
Mean NND (nm)
etoh IAA etoh IAA etoh IAA
CTCF SA1 SA2
j.
100k - 1Mb
1 - 5Mb
SA-CTCF^ΔCoh 1 - 5Mb
EtOH Hi-C
IAA Hi-C
h.
SA1 on CTCF
SA2 on CTCF
Probability
Distance (nm)
EtOH Exp
EtOH Sim
IAA Exp
IAA Sim

Figure 2.

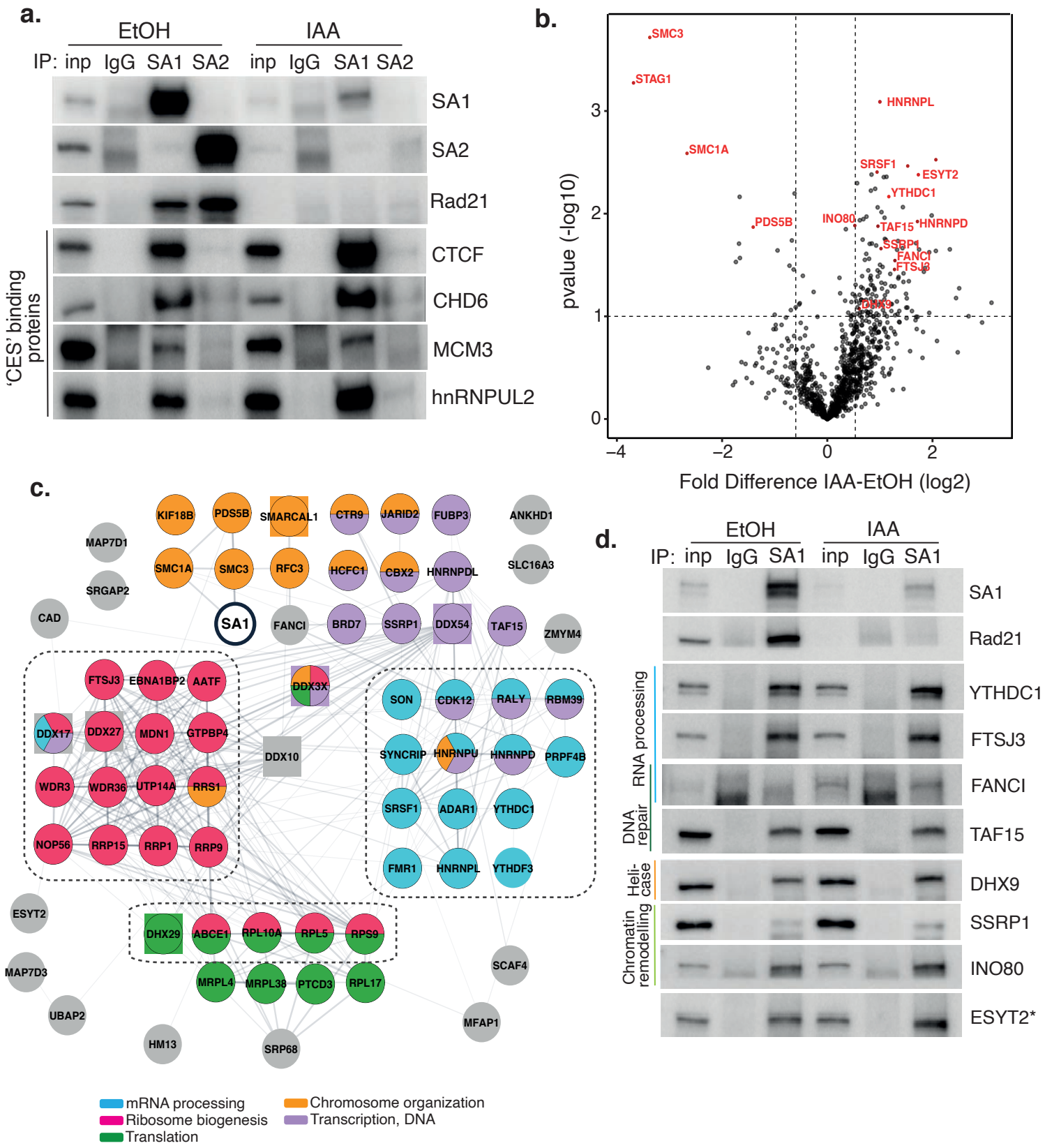
a.
EtOH
IAA
IP: inp IgG SA1 SA2 inp IgG SA1 SA2
SA1
SA2
Rad21
CTCF
CHD6
MCM3
hnRNPUL2
'CES' binding proteins
b.
SMC3
STAG1
SMC1A
PDS5B
HNRNPL
SRSF1
ESYT2
YTHDC1
INO80
TAF15
HNRNPD
SSRP1
FANCI
FTSJ3
DHX9
pvalue (-log10)
Fold Difference IAA-EtOH (log2)
c.
KIF18B
PDS5B
SMARCAL1
CTR9
JARID2
FUBP3
ANKHD1
MAP7D1
SMC1A
SMC3
RFC3
HCFC1
CBX2
HNRNPDL
SLC16A3
SRGAP2
CAD
SA1
FANCI
BRD7
SSRP1
DDX54
TAF15
ZMYM4
FTSJ3
EBNA1BP2
AATF
DDX3X
DDX17
DDX27
MDN1
GTPBP4
DDX10
WDR3
WDR36
UTP14A
RRS1
NOP56
RRP15
RRP1
RRP9
SON
CDK12
RALY
RBM39
SYNCRIP
HNRNPU
HNRNPD
PRPF4B
SRSF1
ADAR1
YTHDC1
FMR1
HNRNPL
YTHDF3
ESYT2
DHX29
ABCE1
RPL10A
RPL5
RPS9
MAP7D3
MRPL4
MRPL38
PTCD3
RPL17
SCAF4
UBAP2
MFAP1
HM13
SRP68
mRNA processing
Ribosome biogenesis
Translation
Chromosome organization
Transcription, DNA
d.
EtOH
IAA
IP: inp IgG SA1 inp IgG SA1
SA1
Rad21
YTHDC1
FTSJ3
FANCI
TAF15
DHX9
SSRP1
INO80
ESYT2*
RNA processing
DNA repair
Heli-case
Chromatin remodelling

Figure 3.

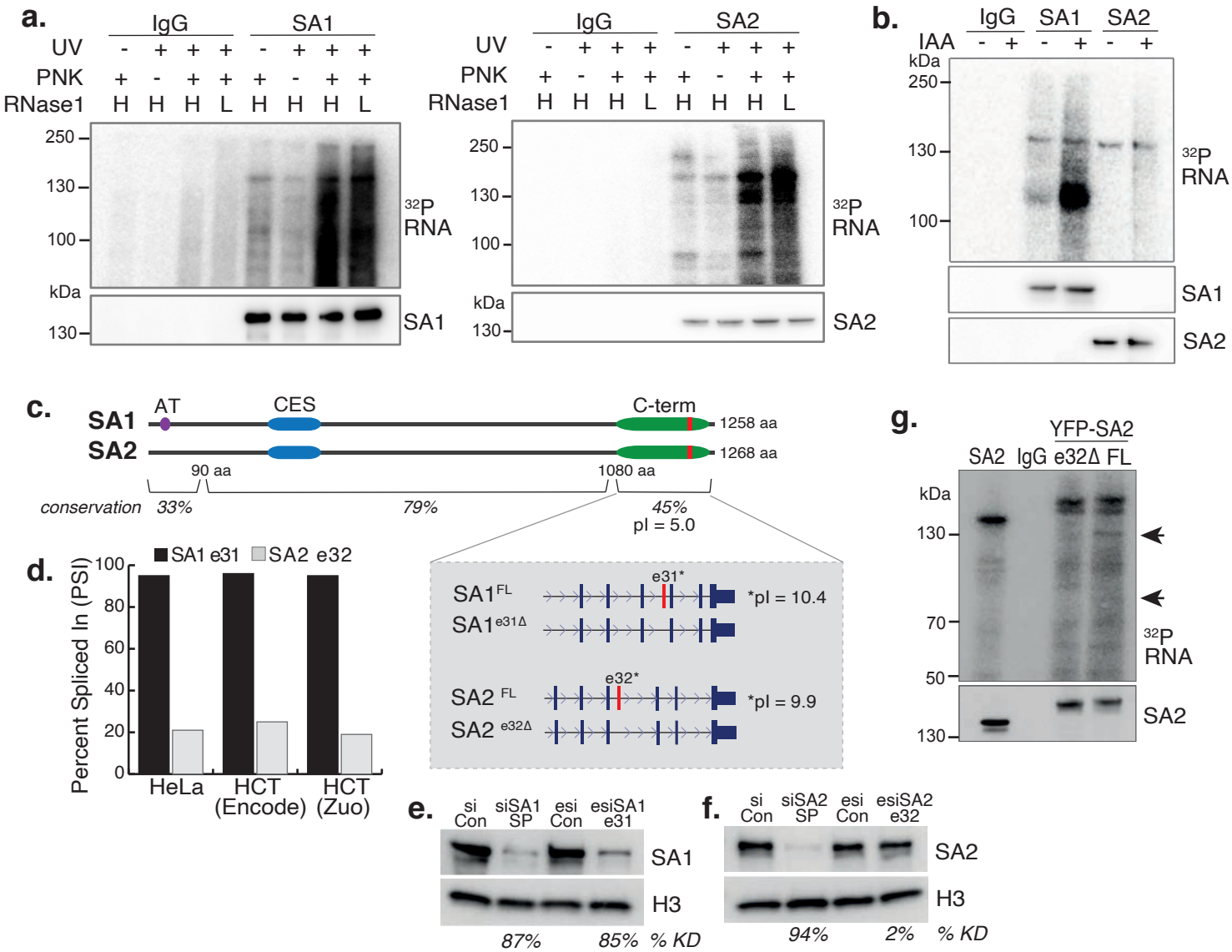
a.
IgG
SA1
UV
PNK
RNase1
250
130
100
kDa
130
32P RNA
SA1
IgG
SA2
SA2
b.
IAA
kDa
250
130
100
32P RNA
SA1
SA2
c.
SA1
SA2
AT
CES
C-term
1258 aa
1268 aa
90 aa
1080 aa
conservation 33%
79%
45%
pI = 5.0
SA1FL
SA1e31Δ
e31*
*pI = 10.4
SA2 FL
SA2 e32Δ
e32*
*pI = 9.9
d.
SA1 e31
SA2 e32
Percent Spliced In (PSI)
100
80
60
40
20
0
HeLa
HCT (Encode)
HCT (Zuo)
e.
si Con
siSA1 SP
esi Con
esiSA1 e31
SA1
H3
87%
85%
% KD
f.
si Con
siSA2 SP
esi Con
esiSA2 e32
SA2
H3
94%
2%
% KD
g.
YFP-SA2
SA2
IgG
e32Δ
FL
kDa
130
70
50
130
32P RNA
SA2

Figure 4.

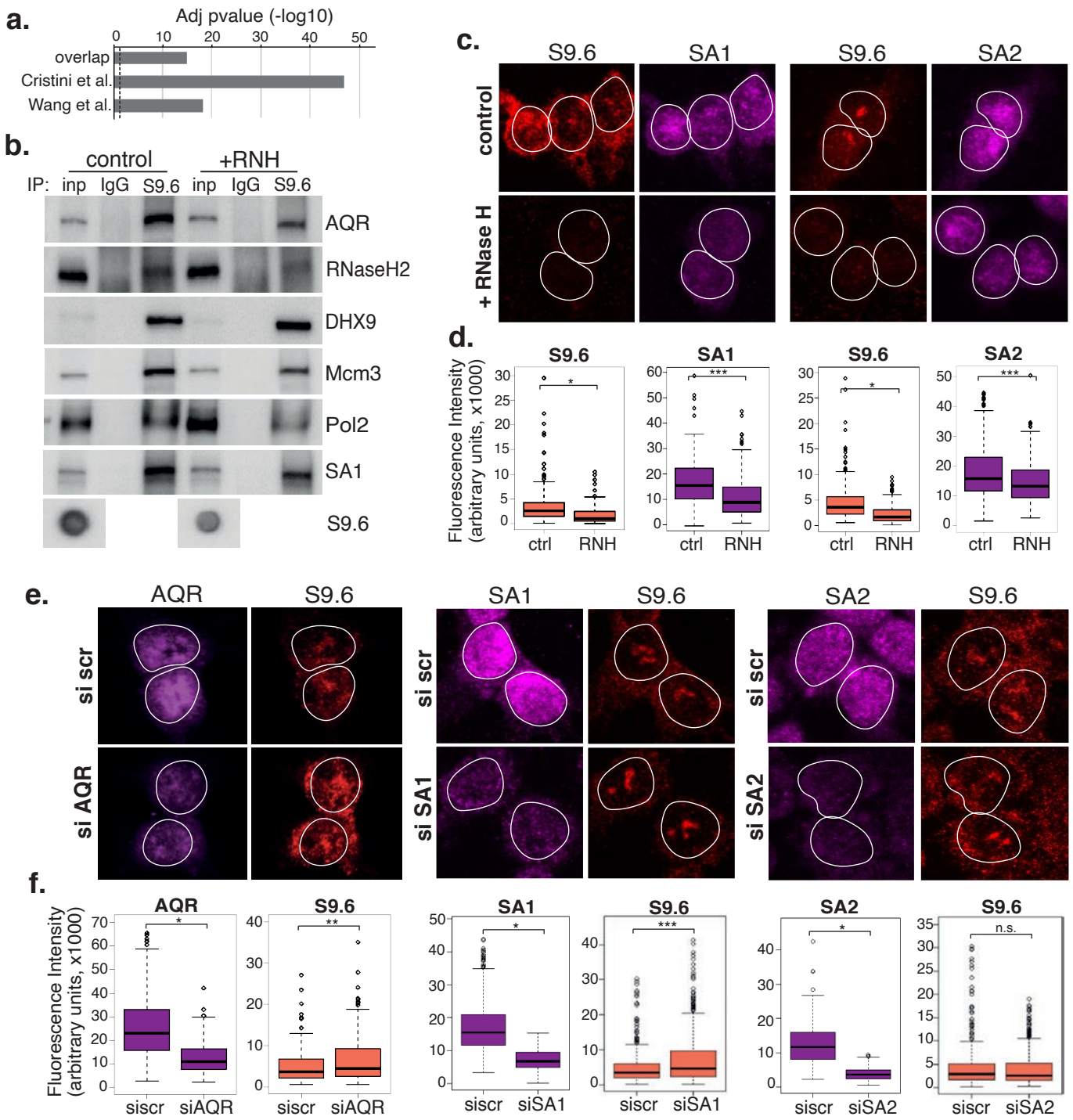
a.
Adj pvalue (-log10)
0 10 20 30 40 50
overlap
Cristini et al.
Wang et al.
b.
control
+RNH
IP: inp IgG S9.6 inp IgG S9.6
AQR
RNaseH2
DHX9
Mcm3
Pol2
SA1
S9.6
c.
S9.6 SA1 S9.6 SA2
control
+ RNase H
d.
Fluorescence Intensity (arbitrary units, x1000)
S9.6 SA1 S9.6 SA2
ctrl RNH
e.
AQR S9.6 SA1 S9.6 SA2 S9.6
si scr
si AQR
si SA1
si SA2
f.
Fluorescence Intensity (arbitrary units, x1000)
AQR S9.6 SA1 S9.6 SA2 S9.6
siscr siAQR siSA1 siSA2
n.s.

Figure 5.

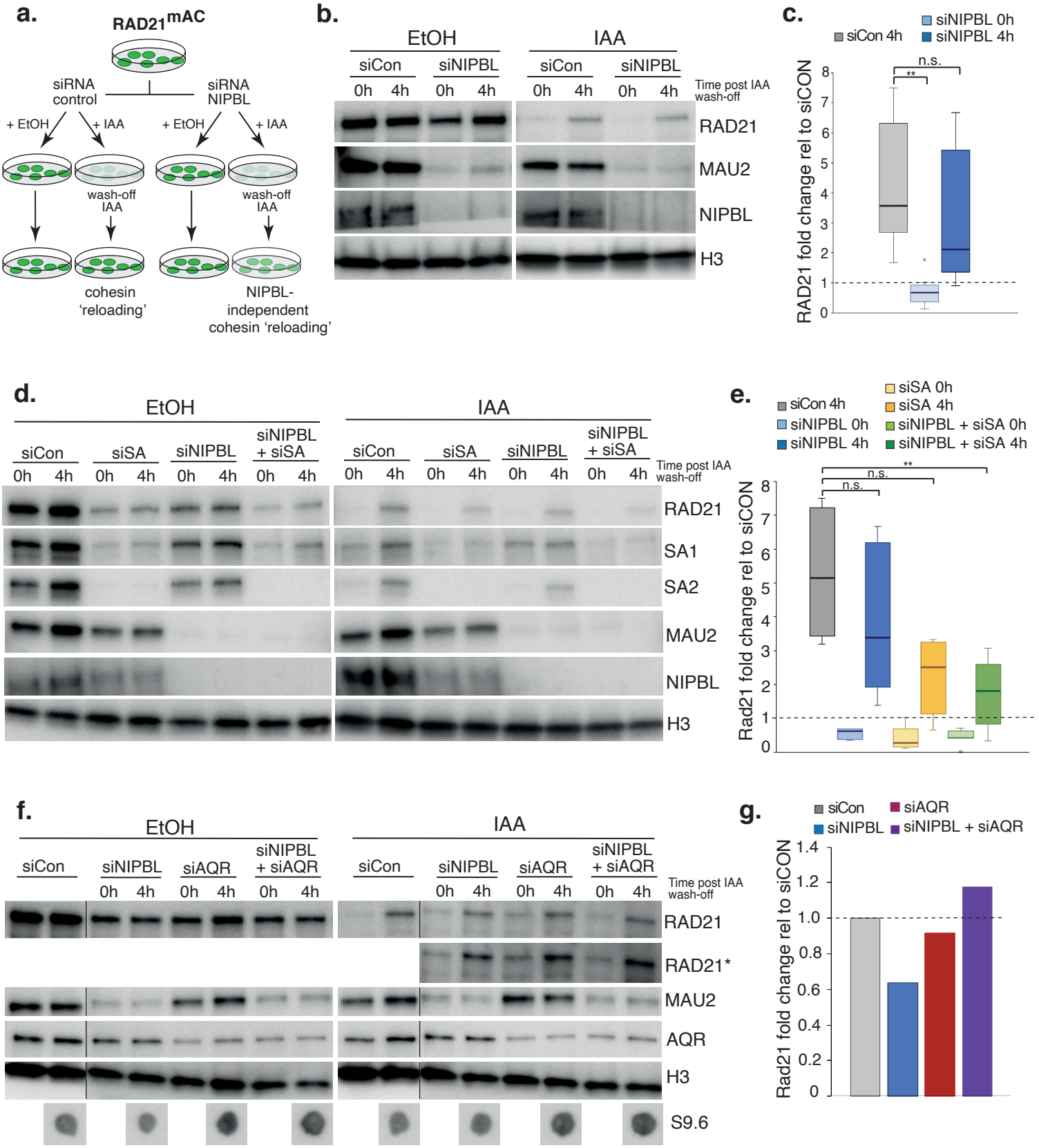
a.
RAD21mAC
siRNA control
siRNA NIPBL
+ EtOH
+ IAA
+ EtOH
+ IAA
wash-off IAA
wash-off IAA
cohesin 'reloading'
NIPBL-independent cohesin 'reloading'
b.
EtOH
IAA
siCon
siNIPBL
siCon
siNIPBL
0h 4h 0h 4h 0h 4h 0h 4h
Time post IAA wash-off
RAD21
MAU2
NIPBL
H3
c.
siCon 4h
siNIPBL 0h
siNIPBL 4h
n.s.
**
RAD21 fold change rel to siCON
d.
EtOH
IAA
siCon
siSA
siNIPBL
siNIPBL + siSA
0h 4h 0h 4h 0h 4h 0h 4h
Time post IAA wash-off
RAD21
SA1
SA2
MAU2
NIPBL
H3
e.
siCon 4h
siNIPBL 0h
siNIPBL 4h
siSA 0h
siSA 4h
siNIPBL + siSA 0h
siNIPBL + siSA 4h
n.s.
n.s.
**
Rad21 fold change rel to siCON
f.
EtOH
IAA
siCon
siNIPBL
siAQR
siNIPBL + siAQR
0h 4h 0h 4h 0h 4h
Time post IAA wash-off
RAD21
RAD21*
MAU2
AQR
H3
S9.6
g.
siCon
siNIPBL
siAQR
siNIPBL + siAQR
Rad21 fold change rel to siCON